Study of Metal Nanoparticle-Catalyzed Hydrogen Generation for Chemical Hydrogen Storage

Aranishi, Kengo

(Degree)
博士（工学）

(Date of Degree)
2014-03-25

(Date of Publication)
2015-03-01

(Resource Type)
doctoral thesis

(Report Number)
甲第6089号

(URL)
https://hdl.handle.net/20.500.14094/D1006089

博 士 論 文

Study of Metal Nanoparticle-Catalyzed Hydrogen Generation for Chemical Hydrogen Storage

金属ナノ粒子触媒を用いた化学的水素貯蔵に関する研究

平成 26 年 1 月

神戸大学大学院工学研究科

荒西　研吾

博 士 論 文

Study of Metal Nanoparticle-Catalyzed Hydrogen Generation for Chemical Hydrogen Storage

金属ナノ粒子触媒を用いた化学的水素貯蔵に関する研究

平成 26 年 1 月

神戸大学大学院工学研究科

荒西　研吾

Acknowledgements

This dissertation is dedicated to all the people who have helped and supported me until now.

The studies described in the present doctoral dissertation have been carried out in the Cooperative Division (located at Kansai Center, National Institute of Advanced industrial Science and Technology (AIST)), Department of Chemical Science and Engineering, Graduate School of Engineering, Kobe University.

I would like to express my deepest gratitude to Professor Qiang Xu for his powerful guidance, inspiring ideas, constructive suggestions, valuable discussions, kind consideration, and for his carefully and critically reading of this dissertation.

I sincerely thank Professor Satoru Nishiyama and Professor Minoru Mizuhata for valuable supports and for critically reading of this dissertation.

I am also deeply indebted to Professor Yusuke Yamada and Professor Yasuo Iizuka for their valuable instruction, valuable supports and kind encouragement.

I am very thankful to Prof. Tomoki Akita, Dr. Hiroshi Shioyama, Dr. Takeyuki Uchida, Dr. Hai-Long Jiang, Dr. Ashish Kumar Shingh, Dr. Qi-Long Zhu, Ms. Yumi Higuchi, Ms. Hitomi Fujii and all the other members in Kansai Center of AIST and Professor Masatake Haruta in Tokyo Metropolitan University for valuable discussions and kind supports.

I am grateful to all the members in Professor Xu's group for their heartwarming kindness.

I thank for financial supports from AIST and Kobe University.

Finally, I appreciate my family for their constant supports and mental encouragements.

Kengo Aranishi
January, 2014
Osaka, Japan

Abstract

This thesis focuses on metal nanoparticle-catalyzed hydrogen generation from liquid-phase chemical hydrogen storage materials. The introduction describes history and development of liquid-phase chemical hydrogen storage materials and their activation by heterogeneous metal nanoparticle catalysts. These catalysts are synthesized with size- and composition-controlled structures, and show synergistic effects between/among metals. In the subsequent chapters, the results obtained in the Ph.D. works are presented, which include the syntheses, characterizations of these functionalized metal nanoparticles and their applications as heterogeneous catalysts for hydrogen generation from hydrolysis of ammonia borane and decomposition of hydrous hydrazine. Triple-layered Au/Co/Fe core-shell NPs were synthesized by noble one-step procedure, which exhibit high activity for hydrolysis of ammonia borane. Monometallic and bimetallic dendrimer-encapsulated nanoparticles (DENs) were synthesized by complexation of metal precursor cations to the internal tertiary amines of hydroxyl terminated, poly-amidoamine (PAMAM) dendrimer followed by reduction step, which are highly efficient for decomposition of hydrous hydrazine and hydrolysis of ammonia borane. The research results of this dissertation are summarized as follows.

(i) One-Step synthesis of magnetically recyclable Au/Co/Fe triple–layered core-shell nanoparticles as highly efficient catalysts for the hydrolytic dehydrogenation of ammonia borane:

Magnetically recyclable Au/Co/Fe core–shell nanoparticles have been successfully synthesized via a one-step *in situ* procedure. Transmission electron microscope, energy

dispersive X-ray spectroscopic, and electron energy-loss spectroscopic measurements revealed that the trimetallic Au/Co/Fe NPs have a triple-layered core–shell structure composed of a Au core, a Co-rich inter-layer, and a Fe-rich shell. The Au/Co/Fe core–shell NPs exhibit much higher catalytic activities for hydrolytic dehydrogenation of ammonia borane than the monometallic (Au, Co, Fe) or bimetallic (AuCo, AuFe, CoFe) counterparts.

(ii) Dendrimer-encapsulated bimetallic Pt-Ni nanoparticles as highly efficient catalysts for hydrogen generation from chemical hydrogen storage materials:

Bimetallic Pt-Ni dendrimer-encapsulated nanoparticles (DENs) with different Pt/Ni ratios have been successfully synthesized through the co-complexation of Pt^{2+} and Ni^{2+} cations to the internal tertiary amine of fourth-generation hydroxyl-terminated poly(amidoamine) dendrimers (G4-OH) followed by coreduction by $NaBH_4$ in aqueous solution. The catalytic activities for the decomposition of hydrous hydrazine and the hydrolysis of ammonia borane over the Pt-Ni DENs have been studied in aqueous solution, and the Pt-Ni DENs show high catalytic performances for these hydrogen-generation reactions. TEM measurements reveal that the size-controlled Pt-Ni NPs, which have an average particle size of 1.1 ± 0.3 nm, are encapsulated in the G4-OH dendrimer.

(iii) Dendrimer-encapsulated Co nanoparticles as high-performance catalyst for hydrolysis of ammonia borane:

Dendrimer-encapsulated Co nanoparticles have been successfully synthesized

through complexation of Co^{2+} cations to internal tertiary amine of sixth-generation hydroxyl-terminated poly(amidoamine) dendrimers (G6-OH(Co_{60})) followed by reduction by both sodium borohydride and ammonia borane in aqueous solution. The highly dispersed G6-OH(Co_{60}) DENs, in which the average diameter of Co NPs is about 1.6 ± 0.4 nm, have been confirmed by TEM analysis. Catalytic activities of G6-OH(Co_{60}) DENs for hydrolysis of AB have been studied in aqueous solution at different reaction temperatures and show a high catalytic performance.

In summary, this dissertation focuses on the synthesis of metal nanoparticles functionalized by stabilizing agents with novel structures, shapes and narrow size distributions, and the investigation of catalytic application to high-performance hydrogen generation from liquid-phase chemical hydrogen storage materials, such as ammonia borane and hydrous hydrazine.

Contents

Chapter 1

General Introduction

In the search for future energy supplies, the application of hydrogen as an energy carrier is seen as a prospective issue. However, the implementation of a hydrogen economy is suffering from several unsolved problems. Particularly challenging is the storage of appropriate amounts of hydrogen. In this context one of the promising hydrogen storage techniques relies on liquid-phase chemical hydrogen storage materials and heterogeneous functional nanoparticles (NPs), which can efficiently catalyze the hydrogen storage materials to generate the hydrogen.

1.1. Liquid-phase Chemical hydrogen storage materials

1.1.1. Background

Chemical hydrogen storage which involves storing of hydrogen in the form of chemical bonds is one of the safe alternatives to physical hydrogen storage [1]. Over the past decades, solid-state hydrogen storage materials have received considerable attention due to their attractive features, such as high hydrogen density, relative stability and safe storability [1–3]. There are many solid-state materials with high hydrogen storage capacities, which, however, display drawbacks, like the high temperature required to desorb hydrogen, slow hydrogen release kinetics and deterioration with successive cycling, different loading/unloading logistics and heat dissipation issues [4].

Thus, the search for safe and efficient liquid-phase hydrogen storage materials to conveniently release hydrogen under mild conditions is desired urgently.

Table 1.1. Hydrogen generation from aqueous NH_3BH_3 catalyzed by noble and non-noble metals.

Catalyst	Catalyst/AB molar ratio (mol mol^{-1})	Maximum H_2/AB ratio (mol mol^{-1})	Time for reaction completion (min)	TOF (min^{-1})	Ref.
2 wt% Ru/γ-Al_2O_3	0.018	3.0	3	56	[22]
Laurate stabilized Ru(0)	0.00125	3.0	22	109	[24]
$[Rh(1,5\text{-}COD)(\mu\text{-}Cl)]_2$	0.018	2.6	15	9.6	[5]
2 wt% Rh/γ-Al_2O_3	0.018	3.0	1.3	128	[22]
Laurate stabilized Rh(0)	0.0025	3.0	6	200	[23]
Zeolite stabilized Rh(0)	0.004	3.0	67	11	[25]
Pd black	0.018	2.6	250	0.6	[5]
2 wt% Pd/γ-Al_2O_3	0.018	2.9	120	1.3	[22]
Pt black	0.018	3.0	12	14	[5]
PtO_2	0.018	3.0	8	21	[5]
2 wt% Pt/C	0.018	3.0	1.5	111	[5]
2 wt% Pt/SiO_2	0.018	3.0	3	56	[22]
2 wt% Pt/γ-Al_2O_3	0.018	3.0	0.8	208	[22]
2 wt%Au/γ-Al_2O_3	0.018	1.9	610	0.2	[22]
In situ Fe particle	0.12	3.0	8	3.1	[26]
10 wt% Co/γ-Al_2O_3	0.018	2.9	70	2.3	[6]
10 wt% Co/C	0.018	2.9	55	2.9	[6]
In situ Co	0.04	3.0	1.7	44	[30]
10 wt% Ni/γ-Al_2O_3	0.018	2.9	65	2.5	[6]
Ni in starch	0.1	3.0	6	5	[27]
Bare Ni NPs	0.1	2.8	11	2.5	[28]
PVP–Ni NPs	0.1	2.7	9	3	[28]
10 wt% Cu/γ-Al_2O_3	0.018	2.9	590	0.3	[6]
$Fe_{0.5}Ni_{0.5}$	0.12	3.0	2.2	11	[29]

1.1.2. Ammonia borane

Ammonia borane (NH_3BH_3, AB) has a hydrogen capacity of 19.6 wt%, exceeding that of gasoline and making it an attractive candidate for chemical hydrogen-storage applications [5–18]. It possesses a volumetric density of 146 g_{H_2} L^{-1} and a gravimetric density of 196 g_{H_2} kg^{-1}. AB is a colorless molecular crystal at room temperature [19] with a density of 0.74 g cm^{-3} [20]. It is stable in air, and soluble in water and other relatively polar solvents [10, 21].

The hydrolysis of AB occurs at an appreciable rate only in the presence of a suitable catalyst at ambient temperature. The hydrolysis reaction can be briefly expressed as follows (Equation 1.1) [5].

$$NH_3BH_3 + 2H_2O \longrightarrow NH_4^+ + BO_2^- + 3H_2 \quad (1.1)$$

The performances of several reported hydrolysis catalysts are summarized in Table 1.1.

1.1.3. Hydrazine

Anhydrous hydrazine (H_2NNH_2), a liquid at room temperature, has a hydrogen content as high as 12.5 wt%. It is a colorless oily liquid at room temperature and used as a monopropellant in satellite propulsion [31]. This compound is hypergolic; it explosively reacts upon exposure to a metal surface.

Hydrous hydrazine, such as hydrazine monohydrate, $H_2NNH_2 \cdot H_2O$, still contains a large amount of hydrogen, 8.0 wt%, which is available for hydrogen generation and is much safer [31], while efforts need to be made from the engineering side to minimize the influence of toxicity.

Table 1.2. Catalytic activities of metal catalysts for decomposition of hydrous hydrazine

Catalyst	Temperature (K)	H_2-selectivityratio (%)	TOF (h^{-1})	Reference
Ru	298	7	———	[41]
Rh	298	43.8	———	[41]
Pd	298	0	———	[41]
Ir	298	7	———	[41]
Pt	298	0	———	[41]
Fe	298	0	———	[41]
Co	298	7	———	[41]
Ni	298	0	———	[41]
Ni	323	33	———	[47]
Cu	298	0	———	[41]
Rh_4Ni	298	100	7.5	[42]
Ni–Pt	298	100	7.9	[44]
Ni–Ir	298	100	3.1	[45]
Ni–Pd	323	80	5.0	[46]
Ni–Fe	298	0	———	[48]
Ni–Fe	343	100	6.3	[48]
Rh–Ni/graphene	298	100	24.5	[49]
Ni–Al hydrotalcite	303	93	2.0	[50]

Hydrazine can be decomposed by supported metals [32], metal nitrides [33, 34], or metal carbides [35, 36] in two ways: incomplete decomposition (Equation 1.2), and the complete decomposition (Equation 1.3).

$$3H_2NNH_2 \longrightarrow 4NH_3 + N_2 \quad (1.2)$$

$$H_2NNH_2 \longrightarrow N_2 + 2H_2 \quad (1.3)$$

The decomposition pathway depends on the catalyst used and reaction applied condtions [32, 34, 36–40]. Notably, generation of only nitrogen as byproduct in addition to hydrogen, which does not need on-board collection for recycling, and easy recharging using the current infrastructure of liquid fuels are distinct advantages of hydrazine. The key to exploit effectively the hydrogen-storage properties of hydrazine is to develop efficient and selective catalysts for H_2 generation from hydrous hydrazine [41–50]. The performances of reported metal catalysts are summarized in Table 1.2.

1.2. Metal nanoparticles

Metal-nanoparticles or clusters, aggregates of several to millions atoms, have been emerging as a new type of important functional material. They exhibit distinct properties (optical, electronic, magnetic, and so on) from those of individual atoms or their bulk counterparts due to the quantum-size and surface effects. More importantly, the properties are usually size- and structure-dependent, which have attracted tremendous research attention from either basic science or application viewpoints during the last two decades [51–53].

1.2.1. Core–shell nanoparticles

Core–shell nanoparticles are in the frontier of advanced materials chemistry among various bimetallic NPs and are of great importance and interest owing to their physical and chemical properties that are strongly dependent on the structure of the core, shell, and interface, and also quite different from those of monometallic counterparts and alloys [54]. This structure dependence opens possibilities for tuning properties by

controlling their chemical composition and the relative sizes of the core and shell.

The successive two-step reduction for core and shell NPs, respectively, is almost universal to prepare core–shell bimetallic NPs. The deposition of the shell metal on the pre-formed core metal NPs seems to be very effective. To this end, however, a second metal must be deposited on the surface of the preformed particles, and the pre-formed metal NPs should be chemically surrounded by the deposited element [55–58].

One-pot synthetic protocol for core–shell NPs is to take advantage of the differences in the reduction potentials of core and shell metal salts, where the key point is to employ a suitable reducing agent. Recently, we synthesized bimetallic Au@Co core-shell NPs via one-step seeding-growth method [59]. For Au@Co core–shell NPs is to take advantage of the different reduction potentials of the two metal salts ($E^{o}_{Co(II)/Co}$= –0.28 eV *vs.* SHE; $E^{o}_{Au(III)/Au}$ = +0.93 eV *vs.*SHE), where NH_3BH_3 as a moderate reducing agent is essential. It is noteworthy that use of a strong reducing agent (*e.g.*, $NaBH_4$) will result in the formation of alloy AuCo NPs, whereas use of a very weak reducing agent (*e.g.*, alcohol) can not yield NPs or give only Au NPs because Co^{2+} can not be reduced [59].

Bi- and multi-metallic NPs are a class of materials that show a combination of properties that are associated with the constituent metals. In many cases, there is a great enhancement in their specific physical/chemical properties, catalytic activities and selectivities owing to a synergistic effect [74–77]. Particularly, core–shell NPs usually exhibit drastic synergestic effect due to their unique electronic strucutures. Reported bimetallic and trimetallic core–shell NPs with synergistic catalytic effects in catalytic reactions are summarized in Table 1.3 [60–73].

Table 1.3. Synergistic effects in catalysis over bimetallic and trimetallic core–shell NPs

Catalyst	NP size (nm)	Catalytic reaction	Reference
Au@Ag/silicate–gel	~16	electro catalytic reduction of H_2O_2	[60]
Ag@Au	4.3	glucose oxidation	[61]
Ag@Au	~2.0	glucose oxidation	[62]
Au@Ag/ZIF-8	3–6	reduction of 4-nitorophenol	[63]
Pd-Au@dendrimer	1–3	hydrogenation of allyl alcohol	[64]
Au@Pd/TiO_2	6.6	oxidation of 1-phenylethanol by H_2O_2	[65]
Rh@Pt	~5	PROX in H_2-rich gas stream	[66]
Pd@Pt dendrites	23.5	oxygen reduction reaction	[67]
Ni@Pt	5.0–5.4	oxygen reduction reaction	[68]
Ag@Ni	~15	dehydrogenation of aqueous $NaBH_4$	[69]
Au@Pd@Pt	~35	methonal electro oxidation	[70]
Au@Pd@Pt	55	formic acid electro oxidation	[71]
Au@Pt@Rh	~3	hydrogenation of methyl acrylate	[72]
Pd@Ag@Rh	~3.5	hydrogenation of methyl acrylate	[73]

1.2.2. Dendrimer-encapsulated nanoparticles

Dendrimers, well-defined highly branched macromolecules composed of a core, divergent branching units, and terminal functional groups, have generated interest because of their great potential in tailoring highly ordered structures and functions [78, 79]. Their name is derived from the Greek word “dendron”, which means “tree” and refers to the distinctive organization of polymer units. Dendrimers are synthesized using a stepwise repetitive reaction sequence that guarantees a very highly monodisperse polymer, with a nearly perfect hyperbranched topology radiating from a central core and grown generation by generation (G). This branching architecture leads to a controlled incremental increase in a dendrimer’s molecular weight, size, and number of surface groups [80, 81].

Poly(amidoamine) (PAMAM) dendrimers are the first synthesized and commercialized dendrimers family, which possessed highly organaized and relatively monodisperse polymers that display a controlled incremental increase in size, molecular weight, and number of surface groups with the increase in generation number (Table 1.4) [81, 82]. PAMAM dendrimers, having an ethylenediamine (EDA) core and hydroxyl terminal functional groups (G*n*-OH, *n* = 0, 1, 2, and 3) are shown in Schemes 1.1 and 1.2.

Table 1.4. Physical Properties of PAMAM–OH Dendrimers (G0-G10) with EDA Core

Gneration number	Number of tertiary amines	Number of surface OH groups	Molecular weight	Diameter (nm)
0	2	4	521	1.5
1	6	8	1438	2.2
2	14	16	3272	2.9
3	30	32	6941	3.6
4	62	64	14279	4.5
5	126	128	28954	5.4
6	254	256	58304	6.7
7	510	512	117005	8.1
8	1022	1024	234407	9.7
9	2046	2048	469210	11.4
10	4094	4096	938816	13.5

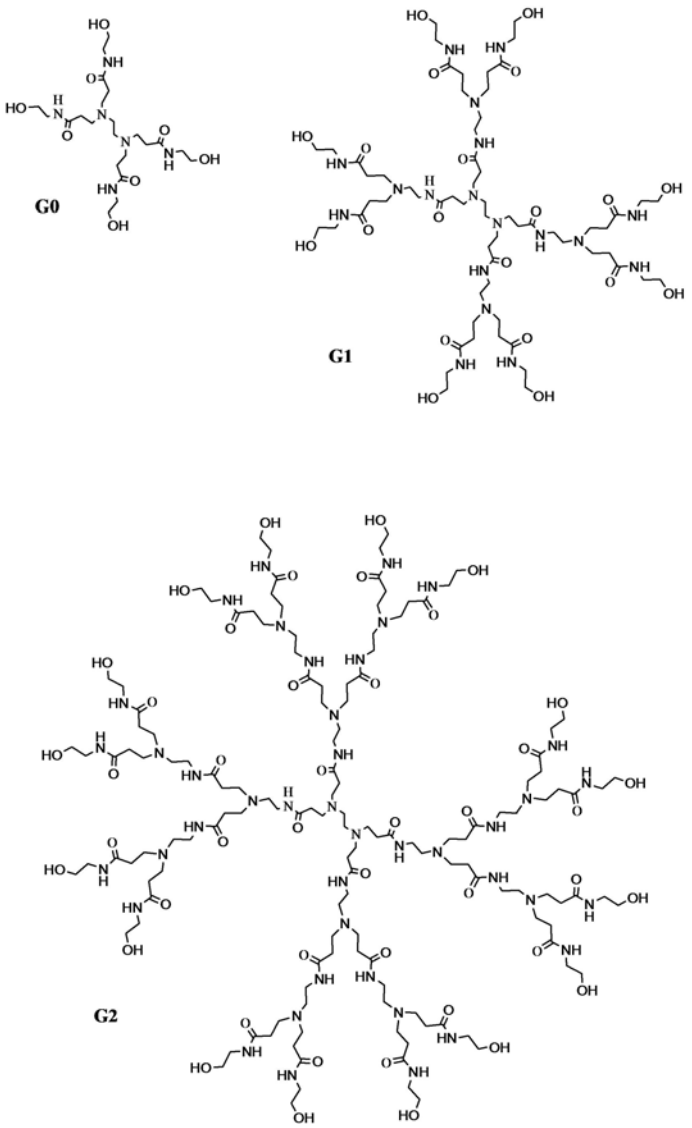

Scheme 1.1. Two-dimensional hydroxyl terminated PAMAM dendrimers (n = 0–2).

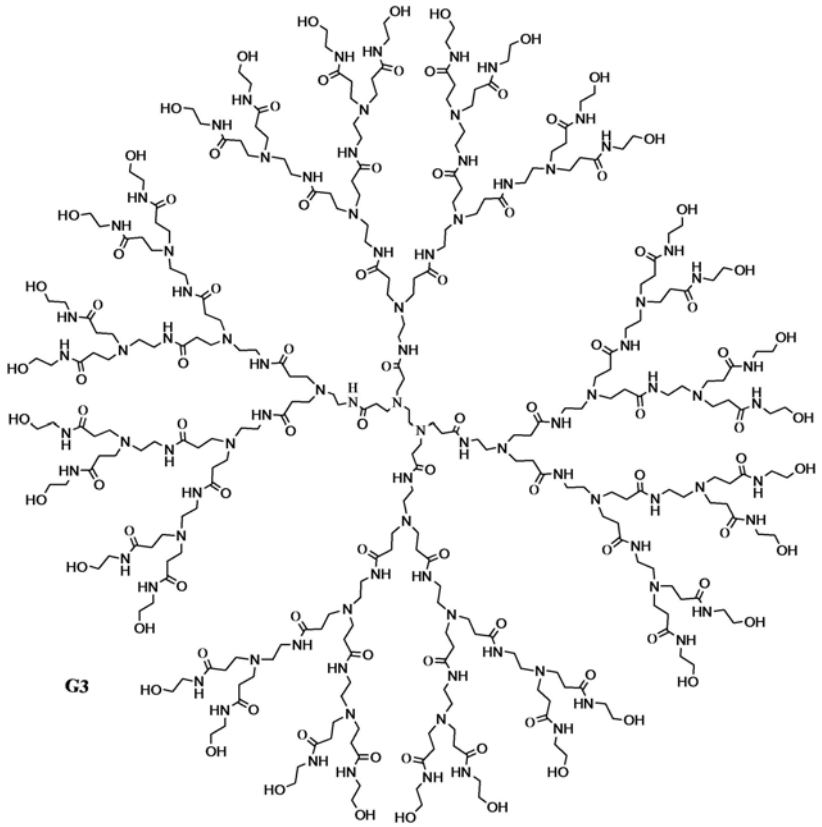

Scheme 1.2. A two-dimensional hydroxyl terminated PAMAM dendrimer (n = 3).

Dendrimers are used as templates to control the size, stability, and solubility of nanoparticles ranging in diameter from less than 1 nm up to 5 nm. Dendrimers are particularly well-suited for hosting metal nanoparticles for the following reasons: (1) the dendrimer templates themselves are of fairly uniform composition and structure, and therefore they yield well-defined nanoparticle replicas; (2) the nanoparticles are stabilized by encapsulation within the dendrimer, and therefore they do not agglomerate; (3) the encapsulated nanoparticles are confined primarily by steric effects, and therefore a substantial fraction of their surface is unpassivated and available to participate in catalytic reactions; (4) the dendrimer branches can be used as selective gates to control access of small molecules (substrates) to the encapsulated (catalytic)

nanoparticles; (5) the terminal groups on the dendrimer periphery can be tailored to control solubility of the hybrid nanocomposite and used as handles for facilitating linking to surfaces and other polymers [83–85].

Dendrimer-encapsulated nanoparticles (DENs), which were first reported by Crooks group in 1998 [83, 84]. These nanocomposite materials are synthesized by complexing metal ions within PAMAM dendrimers and then reducing the composites to yield zerovalent DENs [83, 84]. The driving force for encapsulation of metal ions within PAMAM dendrimers is usually based on covalent bond formation, electrostatic interactions, complexation reactions, or a combination thereof. Metal ions can be complexed exclusively within the interior of PAMAM dendrimers by functionalizing the periphery with noncomplexing entities, such as hydroxyl groups, or by adjusting the solution pH to selectively protonate peripheral amine or acid groups [85].

In summary, this dissertation focuses on the synthesis of metal nanoparticles functionalized by stabilizing agents with novel structures, shapes and narrow size distributions, and the investigation of catalytic application to high-performance hydrogen generation from liquid-phase chemical hydrogen storage materials, such as ammonia borane and hydrous hydrazine.

References

[1] U. Eberle, M. Felderhoff, F. Schüth, *Angew. Chem., Int. Ed.* **2009**, *48*, 6608–6630.

[2] P. Chen, Z. T. Xiong, J. Z. Luo, J. Y. Lin, K. L. Tan, *Nature* **2002**, *420*, 302–304.

[3] B. Bogdanovic, M. Schwickardi, *J. Alloys Compd.* **1997**, *253–254*, 1–9.

[4] W. Grochala, P. P. Edwards, *Chem. Rev.* **2004**, *104*, 1283–1316.

[5] M. Chandra, Q. Xu, *J. Power Sources* **2006**, *156*, 190–194.

[6] Q. Xu, M. Chandra, *J. Power Sources* **2006**, *163*, 364–370.

[7] H. L. Jiang, S. K. Singh, J. M. Yan, X. B. Zhang, Q. Xu, *ChemSusChem* **2010**, *3*, 541–549.

[8] P. Wang, X. D. Kang, *Dalton Trans.* **2008**, 5400–5413.

[9] T. Umegaki, J. M. Yan, X. B. Zhang, H. Shioyama, N. Kuriyama, Q. Xu, *Int. J. Hydrogen Energy* **2009**, *34*, 2303–2311.

[10] F. H. Stephens, V. Pons, R. T. Baker, *Dalton Trans.* **2007**, 2613–2626.

[11] C. W. Hamilton, R. T. Baker, A. Staubitz, I. Manners, *Chem. Soc. Rev.* **2009**, *38*, 279–293.

[12] H. W. Langmi, G. S. McGrady, *Coord. Chem. Rev.* **2007**, *251*, 925–935.

[13] Q. Xu, M. Chandra, *J. Alloys Compd.* **2007**, *446–447*, 729–732.

[14] A. Gutowska, L. Li, Y. Shin, C. M. Wang, X. S. Li, J. C. Linehan, R. S. Smith, B. D. Kay, B. Schmid, W. Shaw, M. Gutowski, T. Autrey, *Angew. Chem., Int. Ed.* **2005**, *44*, 3578–3582.

[15] Z. Li, G. Zhu, G. Lu, S. Qiu, X. Yao, *J. Am. Chem. Soc.* **2010**, *132*, 1490–1491.

[16] F. H. Stephens, R. T. Baker, M. H. Matus, D. J. Grant, D. A. Dixon, *Angew. Chem., Int. Ed.* **2007**, *46*, 746–749.

[17] T. B. Marder, *Angew. Chem., Int. Ed.* **2007**, *46*, 8116–8118.

[18] U. B. Demirci, P. Miele, *Energy Environ. Sci.* **2009**, *2*, 627–637.

[19] R. Custelcean, Z. A. Dreger, *J. Phys. Chem. B* **2003**, *107*, 9231–9235.

[20] S. G. Shore, R. W. Parry, *J. Am. Chem. Soc.* **1958**, *80*, 8–12.

[21] A. T. Raissi, *Hydrogen From Ammonia and Ammonia–Borane Complex for Fuel Cell Applications*, Proceedings of the 2002 US DOE Hydrogen Program Review,

2002.

[22] M. Chandra, Q. Xu, *J. Power Sources* **2007**, *168*, 135–142.

[23] F. Durap, M. Zahmakıran, S. Özkar, *Appl. Catal. A*, **2009**, *369*, 53–59.

[24] F. Durap, M. Zahmakıran, S. Özkar, *Int. J. Hydrogen Energy* **2009**, *34*, 7223–7230.

[25] M. Zahmakıran, S. Özkar, *Appl. Catal. B* **2009**, *89*, 104–110.

[26] J. M. Yan, X. B. Zhang, S. Han, H. Shioyama, Q. Xu, *Angew. Chem., Int. Ed.* **2008**, *47*, 2287–2289.

[27] J. M. Yan, X. B. Zhang, S. Han, H. Shioyama, Q. Xu, *Inorg. Chem.* **2009**, *48*, 7389–7393.

[28] T. Umegaki, J. M. Yan, X. B. Zhang, H. Shioyama, N. Kuriyama, Q. Xu, *Int. J. Hydrogen Energy* **2009**, *34*, 3816–3822.

[29] J. M. Yan, X. B. Zhang, S. Han, H. Shioyama, Q. Xu, *J. Power Sources* **2009**, *194*, 478–481.

[30] T. Umegaki, J. M. Yan, X. B. Zhang, H. Shioyama, N. Kuriyama, Q. Xu, *J. Power Sources* **2010**, *195*, 8209–8214.

[31] E. W. Schmidt, *Hydrazine and Its Derivatives: Preparation, Properties, Applications*, 2nd ed., John Wiley & Sons, New York, **1984**.

[32] M. Zheng, R. Cheng, X. Chen, N. Li, L. Li, X. Wang, T. Zhang, Int. *J. Hydrogen Energy* **2005**, *30*, 1081–1089.

[33] X. Chen, T. Zhang, L. Xia, T. Li, M. Zheng, Z. Wu, X. Wang, Z. Wei, Q. Xin, C. Li, *Catal. Lett.* **2002**, *79*, 21–25.

[34] M. Zheng, X. Chen, R. Cheng, N. Li, J. Sun, X. Wang, T. Zhang, *Catal. Commun.* **2006**, *7*, 187–191.

[35] X. Chen, T. Zhang, P. Ying, M. Zheng, W. Wu, L. Xia, T. Li, X. Wang, C. Li,

Chem. Commun. **2002**, 288–289.

[36] J. B. O. Santos, G. P. Valença, J. A. J. Rodrigues, *J. Catal.* **2002**, *210*, 1–6.

[37] X. Chen, T. Zhang, M. Zheng, Z. Wu, W. Wu, C. Li, *J. Catal.* **2004**, *224*, 473–478.

[38] Y. K. Al-Haydari, J. M. Saleh, M. H. Matloob, *J. Phys. Chem.* **1985**, *89*, 3286–3290.

[39] D. J. Alberas, J. Kiss, Z. M. Liu, J. M. White, *Surf. Sci.* **1992**, *278*, 51–61.

[40] J. Prasad, J. L. Gland, *Langmuir* **1991**, *7*, 722–726.

[41] S. K. Singh, X. B. Zhang, Q. Xu, *J. Am. Chem. Soc.* **2009**, *131*, 9894–9895.

[42] S. K. Singh, Q. Xu, *J. Am. Chem. Soc.* **2009**, *131*, 18032–18033.

[43] S. J. Cho, J. Lee, Y. S. Lee, D. P. Kim, *Catal. Lett.* **2006**, *109*, 181–187.

[44] S. K. Singh, Q. Xu, *Inorg. Chem.* **2010**, *49*, 6148–6152.

[45] S. K. Singh, Q. Xu, *Chem. Commun.* **2010**, *46*, 6545–6547.

[46] S. K. Singh, Y. Iizuka, Q. Xu, *Int. J. HydrogenEnergy* **2011**, *36*, 11794–11801.

[47] S. K. Singh, Z. H. Lu, Q. Xu, *Eur. J. Inorg. Chem.* **2011**, 2232–2237.

[48] S. K. Singh, A. K. Singh, K. Aranishi, Q. Xu, *J. Am. Chem. Soc.* **2011**, *133*, 19638–19641.

[49] J. Wang, X. B. Zhang, Z. L. Wang, L. M. Wang, Y. Zhang, *Energy Environ. Sci.* **2012**, *5*, 6885–6888.

[50] L. He, Y. Huang, A. Wang, X. Wang, X. Chen, J. J. Delgado, T. Zhang, *Angew. Chem., Int. Ed.* **2012**, *51*, 6191–6194.

[51] M. Haruta, N. Yamada, T. Kobayashi, S. Lijima, *J. Catal.* **1989**, *115*, 301–309.

[52] X. Wang, J. Zhuang, Q. Peng, Y. D. Li, *Nature* **2005**, *437*, 121–124.

[53] Y. Xia, Y. Xiong, B. Lim, S. E. Skrabalak, *Angew. Chem., Int. Ed.* **2009**, *48*, 60–103.

[54] J. Wang, X. C. Zeng, *in Core–Shell Magnetic Nanoclusters in Nanoscale Magnetic Materials and Applications* (eds. J. P. Liu, E. Fullerton, O. Gutfleisch, D. J. Sellmyer), Springer Science & Business Media, Inc., **2009**, pp. 35–65.

[55] B. Lim, H. Kobayashi, T. Yu, J. Wang, M. J. Kim, Z.-Y. Li, M. Rycenga, Y. Xia, *J. Am. Chem. Soc.* **2010**, *132*, 2506–2507.

[56] M. Tsuji, D. Yamaguchi, M. Matsunaga, M. *J. Alam, Cryst. Growth Des.* **2010**, *10*, 5129–5135.

[57] M. Tsuji, M. Ogino, M. Matsunaga, N. Miyamae, R. Matsuo, M. Nishio, M. J. Alam, *Cryst. Growth Des.* **2010**, *10*, 4085–4090.

[58] A. Śanchez-Iglesias, E. Carbó-Argibay, A. Glaria, B. Rodríguez-González, J. Pérez-Juste, I. Pastoriza-Santos, L. M. Liz-Marzán, *Chem.–Eur. J.* **2010**, *16*, 5558–5563.

[59] J. M. Yan, X. B. Zhang, T. Akita, M. Haruta, Q. Xu, *J. Am. Chem. Soc.* **2010**, *132*, 5326–5327.

[60] S. Manivannan, R. Ramaraj, *J. Chem. Sci*. **2009**, *121*, 735–743.

[61] S. Tokonami, N. Morita, K. Takasaki, N. Toshima, *J. Phys. Chem. C* **2010**, *114*, 10336–10341.

[62] H. Zhang, J. Okuni, N. Toshima, *J. Colloid Interface Sci.* **2011**, *354*, 131–138.

[63] H. L. Jiang, T. Akita, T. Ishida, M. Haruta, Q. Xu, *J. Am. Chem. Soc.* **2011**, *133*, 1304–1306.

[64] R. W. J. Scott, O. M. Wilson, S.-K. Oh, E. A. Kenik, R. M. Crooks, *J. Am. Chem. Soc.* **2004**, *126*, 15583–15591.

[65] A. J. Frank, J. Rawski, K. E. Maly, V. Kitaev, *Green Chem.* **2010**, *12*, 1615–1622.

[66] S. Alayoglu, B. Eichhorn, *J. Am. Chem. Soc.* **2008**, *130*, 17479–17486.

[67] B. Lim, M. Jiang, P. H. C. Camargo, E. C. Cho, J. Tao, X. Lu, Y. Zhu, Y. Xia, *Science* **2009**, *324*, 1302–1305.

[68] Y. Chen, F. Yang, Y. Dai, W. Wang, S. Chen, *J. Phys. Chem. C*, **2008**, *112*, 1645–1649.

[69] H. Guo, Y. Chen, X. Chen, R. Wen, G.-H. Yue, D. L. Peng, *Nanotechnology* **2011**, *22*, 195604.

[70] L. Wang, Y. Yamauchi, *J. Am. Chem. Soc.* **2010**, *132*, 13636–13638.

[71] P. P. Fang, S. Duan, X. D. Lin, J. R. Anema, J. F. Li, O. Buriez, Y. Ding, F. R. Fan, D. Y. Wu, B. Ren, Z. L. Wang, C. Amatore, Z. Q. Tian, *Chem. Sci.* **2011**, *2*, 531–539.

[72] N. Toshima, R. Ito, T. Matsushita, Y. Shiraishi, *Catal. Today* **2007**, *122*, 239–244.

[73] T. Matsushita, Y. Shiraishi, S. Horiuchi, N. Toshima, *Bull. Chem. Soc. Jpn*. **2007**, *80*, 1217–1225.

[74] D. S. Wang, Y. Li, *Adv. Mater*. **2011**, *23*, 1044–21060.

[75] T. Krenke, E. Duman, M. Acet, E. F. Wassermann, X. Moya, L. Manosa, A. Planes, *Nat. Mater.* **2005**, *4*, 450–454.

[76] K. Gschneidner, A. Russell, A. Pecharsky, J. Morris, Z. H. Zhang, T. Lograsso, D. Hsu, C. H. C. Lo, Y. Y. Ye, A. Slager, D. Kesse, *Nat. Mater*. **2003**, *2*, 587–591.

[77] H.-L. Jiang, Q. Xu, *J. Mater. Chem*. **2011**, *21*, 13705–13725.

[78] D. A. Tomalia, A. M. Naylor, W. A. Goddard III, *Angew. Chem. Int. Ed. Engl*. **1990**, *29*, 138–175.

[79] J. F. G. A. Jansen, E. M. M. de Brabander-van den Berg, E. W. Meijer, *Science* **1994**, *266*, 1226–1229.

[80] J. F. G. A. Jansen, E. W. Meijer, *J. Am. Chem. Soc.* **1995**, *117*, 4417–4418.

[81] S. H. Medina, M. E. H. El-Sayed, *Chem. Rev.* **2009**, *109*, 3141–3157.

[82] R. Esfand, D. A. Tomalia, *Drug DiscoVery Today* **2001**, *6*, 427–436.

[83] M. Zhao, L. Sun, R. M. Crooks, *J. Am. Chem. Soc.* **1998**, *120*, 4877–4878.

[84] R. M. Crooks, M. Zhao, L. Sun, V. Chechik, L. K. Yeung, *Acc. Chem. Res.* **2001**, *34*, 181–190.

[85] V. Chechik, M. Zhao, R. M. Crooks, *J. Am. Chem. Soc.* **1999**, *121*, 4910–4911.

Chapter 2

One-Step synthesis of magnetically recyclable Au/Co/Fe triple–layered core-shell nanoparticles as highly efficient catalysts for the hydrolytic dehydrogenation of ammonia borane

2.1. Introduction

Heterometallic nanoparticles (NPs) have attracted growing attention in recent years owing to their unique and novel properties, which are often very different from those of the monometallic counterparts [1–16]. The incorporation of magnetic elements in NPs will expand their applications to biomedical operations, information storage, and heterogeneous catalysis [15, 16]. Therefore, studies of the synthesis and applications of magnetic alloy NPs are of great interest in terms of seeking synergistic structural and electronic effects combined with the intrinsic properties of the magnetic element. There have been a considerable number of investigations of core–shell structured bimetallic magnetic NPs [16–18], whereas magnetic core–shell NPs with a triple-layered structure are, to the best of our knowledge, rare [18–20]. Triple-layered trimetallic NPs might have superior physicochemical (especially catalytic) performances to their monometallic/bimetallic counterparts because their electronic structures are more tunable [6, 21]. Toshima and coworkers have fabricated ~3 nm Au/Pt/Rh trimetallic NPs by simple mixing of bimetallic Au/Pt NPs and monometallic Rh NPs [18]. Sun and coworkers have obtained ~6 nm Pd/Au/FePt core–shell NPs via a multi-step synthetic approach [19]. Yamauchi and coworkers have reported the one-step synthesis of

multifunctional Au/Pd/Pt core–shell NPs with an average particle diameter of 35 nm [20]. Developing a facile one-step route to construct triple-layered nonnoble metal-containing core–shell NPs with small particle sizes and with high catalytic activities still remains a considerable challenge, however. Currently, a great deal of work has been devoted to the development of effective hydrogen storage materials for hydrogen fuel cells and hydrogen energy systems. Ammonia borane (NH_3BH_3, AB) has a hydrogen capacity as high as 19.6 wt%, which exceeds that of gasoline, and is accordingly an attractive candidate for chemical hydrogen-storage [22–36]. Hydrogen can be generated by thermal decomposition of AB [23–26], but catalytic hydrolysis provides an alternative route for hydrogen generation under milder conditions [12, 27–36]. One of the major requirements for practical application of the catalytic decomposition is to develop efficient, economical, and easily recyclable catalysts. Herein, we report a facile one-step seeding-growth method for preparing magnetically recyclable Au/Co/Fe triple-layered core–shell NPs around 10 nm in diameter under ambient conditions. Compared with their monometallic and bimetallic counterparts, the Au/Co/Fe triple-layered core–shell NPs exhibit remarkably enhanced catalytic activity for the hydrolytic dehydrogenation of aqueous AB.

2.2. Experimental details

2.2.1. Chemicals

Ammonia borane (NH_3BH_3, AB, JSC Aviabor, 97%), iron (III) chloride hexahydrate ($FeCl_3 \cdot 6H_2O$, Sigma–Aldrich Japan, 99.0%), cobalt (II) chloride hexahydrate ($CoCl_2 \cdot 6H_2O$, Wako Pure Chemical Industries, Ltd., > 99%), hydrogen tetrachloroaurate (III) tetrahydrate($HAuCl_4 \cdot 4H_2O$, Wako Pure Chemical Industries, Ltd.,

> 99%), polyvinylpyrrolidone K 30 (PVP, $(C_6H_9NO)_n$, Mw: av. 40,000, Tokyo Chemical Industry Co., Ltd.), platinum (IV) dioxide ($PtO_2 \cdot nH_2O$, Mitsuwa Chemicals Co., Ltd., Pt > 78.8%), and ethanol (CH_3CH_2OH, Kishida Chemical Co., Ltd., > 99.8%) were used as received. Deionized H_2O with a specific resistance of 17.5 MΩ cm was obtained by reversed osmosis followed by ion-exchange and filtration (RFD250NB, Toyo Roshi Kaisha, Ltd., Japan).

2.2.2. Physical characterization

Ultraviolet-visible (UV–Vis) absorption spectra were recorded on a Shimadzu UV-2550 spectrophotometer in the wavelength range 300–800 nm and corrected using aqueous PVP (1 wt%) solution as background absorption. Transmission electron microscope (TEM, JEOL JEM-3000F), high-angle annular dark-field scanning TEM (HAADF-STEM), energy-dispersive X-ray spectroscopy (EDS), and electron energy-loss spectroscopy (EELS) were used for the determination of detailed microstructure and composition. The TEM (HAADF-STEM, EDS, EELS) samples were prepared by depositing one or two droplets of the NPs suspended in the reaction solution onto amorphous carbon-coated copper grids, which were then dried in an argon atmosphere. Powder X-ray diffraction (XRD) was performed on a Rigaku RINT-2000 X-ray diffractometer with Cu *K*α radiation. A glass substrate holding the powder sample was covered by an adhesive tape on the surface to prevent the sample from exposure to air during the measurements. Mass analysis of the generated gases was performed using a Balzers Prisma QMS 200 mass spectrometer.

2.2.3. Synthesis of Au/Co/Fe triple-layered core–shell nanoparticles

In a typical experiment, 5.0 mg of $HAuCl_4 \cdot 4H_2O$ (0.012 mmol), 2.9 mg of

$CoCl_2 \cdot 6H_2O$ (0.012 mmol), and 48.1 mg of $FeCl_3 \cdot 6H_2O$ (0.176 mmol) were dissolved along with PVP (100 mg) in 10.0 mL of water (giving a molar ratio of Au:Co:Fe = 6:6:88). The solution of metal salt precursors was shaken (220 r/min) at room temperature for 2 min and then 55.0 mg of NH_3BH_3 was added while shaking. Magnetic stirring was not employed because of the aggregation of the prepared magnetic particles caused by the strong magnet. The synthetic progress was monitored by UV–Vis spectroscopy. The as-prepared samples were used for XRD and TEM measurements.

2.2.4. Synthesis of bimetallic nanoparticles

A similar procedure to that described above for the preparation of triple-layered NPs was employed. For Au/Fe NPs, 5.0 mg of $HAuCl_4 \cdot 4H_2O$ (0.012 mmol) and 48.1 mg of $FeCl_3 \cdot 6H_2O$ (0.176 mmol) were used. For the synthesis of Au/Co NPs, 5.0 mg of $HAuCl_4 \cdot 4H_2O$ (0.012 mmol) and 2.9 mg of $CoCl_2 \cdot 6H_2O$ (0.012 mmol) were used. For the synthesis of Co/Fe NPs, 2.9 mg of $CoCl_2 \cdot 6H_2O$ (0.012 mmol) and 48.1 mg of $FeCl_3 \cdot 6H_2O$ (0.176 mmol) were used.

2.2.5. Synthesis of monometallic Au, Co, and Fe nanoparticles

5.0 mg of $HAuCl_4$ (0.012 mmol), 2.9 mg of $CoCl_2$ (0.012 mmol), and 48.1 mg of $FeCl_3$ (0.176 mmol) were used for the syntheses of Au NPs, Co NPs, and Fe NPs, respectively. The procedure was similar to those for the triple-layered NPs and the bimetallic NPs.

2.2.6. Catalytic hydrolysis of ammonia borane

The *in situ* synthesized mono- and heterometallic NPs were directly used for

catalytic hydrolysis of AB. Typically, 55.0 mg of AB was fed into a two-necked round-bottom flask, with one neck connected to a gas burette, and the other connected to a pressure-equalizing funnel to introduce the metal salt precursor(s) in 1 wt% aqueous PVP solution (10.0 mL). The reaction started when the starting material in aqueous PVP solution was added to AB with vigorous shaking. The evolution of H_2, which was identified by mass spectrometry, was monitored using a gas burette. The reactions were carried out at room temperature under ambient atmosphere (Equation 2.1).

$$NH_3BH_3 + 2H_2O \longrightarrow NH_4^+ + BO_2^- + 3H_2 \quad (2.1)$$

2.2.7. Durability tests of Au/Co/Fe triple-layered core–shell nanoparticles

The prepared Au/Co/Fe triple-layered core–shell NPs were isolated from the reaction solution by a magnet when hydrogen generation was complete. A new catalytic run was started by adding an additional equivalent amount of aqueous AB solution (55.0 mg AB in 10.0 mL of water) and the evolution of gas was monitored as described above.

2.2.8. Heat treatment of Au/Co/Fe triple-layered core–shell nanoparticles

The synthesized Au/Co/Fe triple-layered core–shell NPs were washed twice by water and once with ethanol. The sample was dried in a vacuum oven at room temperature and was then transferred into a furnace where a continuous He gas flow was introduced at the rate of 90 mL/min. The furnace temperature was elevated to 873 K and maintained at this value for 5 h. XRD patterns of the material before and after heat treatment were recorded.

2.3. Results and discussion

The one-step synthetic method for the Au/Co/Fe triplelayered core–shell NPs involved exposing a mixture of Au^{3+}, Co^{2+}, and Fe^{3+} precursors to the reducing agent at the same time. The basic concept is to take advantage of the difference in the reduction potentials of the three soluble metal cations ($E^{o}_{Fe(III)/Fe(II)}$ = +0.77 V *vs*. the standard hydrogen electrode (SHE); $E^{o}_{Fe(II)/Fe}$ = –0.44 V *vs*. SHE; $E^{o}_{Co(II)/Co}$ = –0.28 V *vs*. SHE; $E^{o}_{Au(III)/Au}$ = +0.93 V *vs*. SHE), which are a measure of their tendency to undergo reduction. Alcohols and ascorbic acid have been used as the reducing agents for the one-step synthesis of core–shell NPs of three noble metals [18, 20], but these are not applicable to nonnoble metal-containing trimetallic core–shell NPs. In this work, AB was employed as the reducing agent, since the core Au NPs can be formed within a few seconds and then serve as *in situ* seeds for the successive catalytic reduction leading to the growth of the outer layers. Without Au cores, Fe and Co NPs cannot be formed because of their lower standard reduction potentials and the weak reduction capability of AB (even though Fe^{3+} can be reduced to Fe^{2+}). Formation of the Au cores leads to the slow release of H_2, inducing the reduction of Co^{2+} and growth of a Co-rich layer. Finally, the presence of the Au/Co core–shell NPs results in the rapid generation of H_2, which reduces Fe^{2+} to form a Fe-rich outer shell. The Au/Co/Fe triple-layered core–shell NPs are thus formed through successive reduction processes. On the basis of the difference in the reduction potentials of the three metal ions, a moderate reducing agent such as AB is essential.

The synthesis process can be monitored by the evolution of the solution color (Figure 2.1). Under typical experimental conditions, once the aqueous solution of

$HAuCl_4$, $CoCl_2$, and $FeCl_3$ with a molar ratio of 6:6:88 in the presence of PVP (1 wt%) as the stabilizing agent was mixed with the solid AB, the color of the mixture immediately changed from its original light-yellow color (Figure 2.1a) to wine-red (Figure 2.1b) in a few seconds, indicating that Au^{3+} cations are preferentially reduced to Au^0 NPs prior to reduction of Co^{2+} and Fe^{3+} cations. Then the Au NPs serve as seeds for successive growth of Co and Fe shells during the H_2 generation. Accordingly, the solution color darkened to black within 1 min (Figure 2.1c). Based on this color evolution and their intrinsic difference in reduction potentials, we can reasonably assume that the resulting particles have a core–shell architecture.

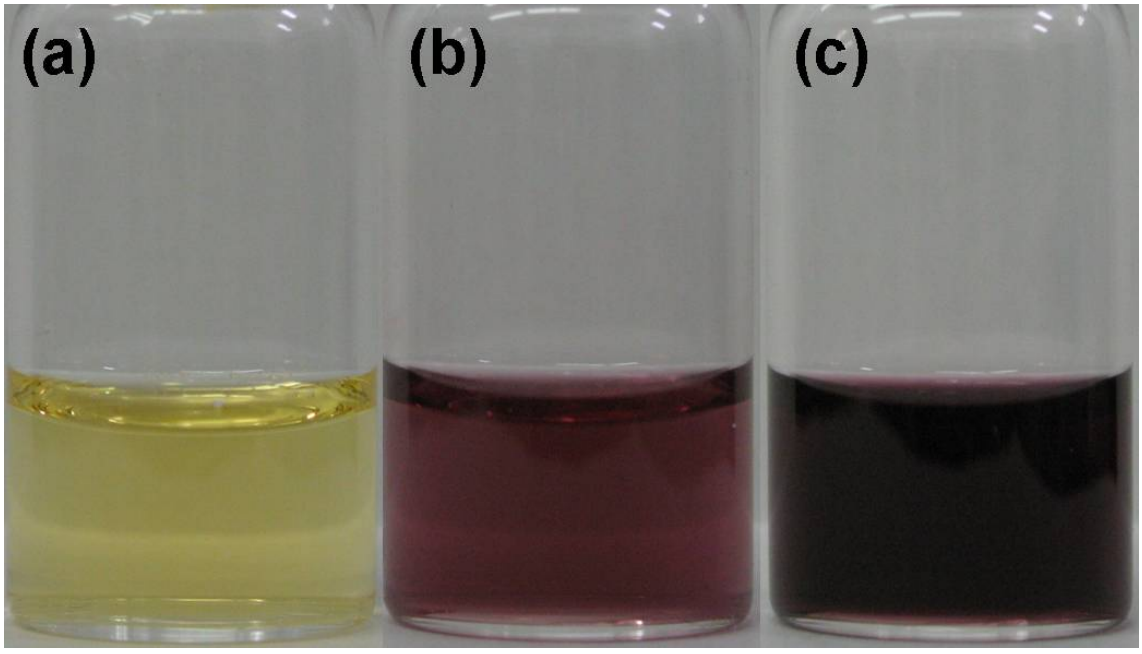

Figure 2.1. Color evolution during the formation of Au/Co/Fe core–shell NPs via a one-step seeding-growth method at room temperature. (a) Before, and (b) 10 s and (c) 1 min after adding AB to the aqueous PVP solution containing Au^{3+}, Co^{2+}, and Fe^{3+} precursors.

This assumption has been confirmed by monitoring the UV–Vis spectra (Figure 2.2).

No peaks can be observed before the addition of AB (Figure 2.2a), whereas 10 s after introducing AB a distinct peak appears at 540 nm (Figure 2.2b). This peak arises from the surface plasmon absorption of Au NPs. Then this characteristic peak broadens quickly and disappears completely in 2 min (Figure 2.2c) due to the broad and strong absorption of the Co and Fe layers in the same spectral region with Au cores. The consistent evolution of color and UV–Vis spectra present strong evidence for the formation of a Au/Co/Fe core–shell architecture.

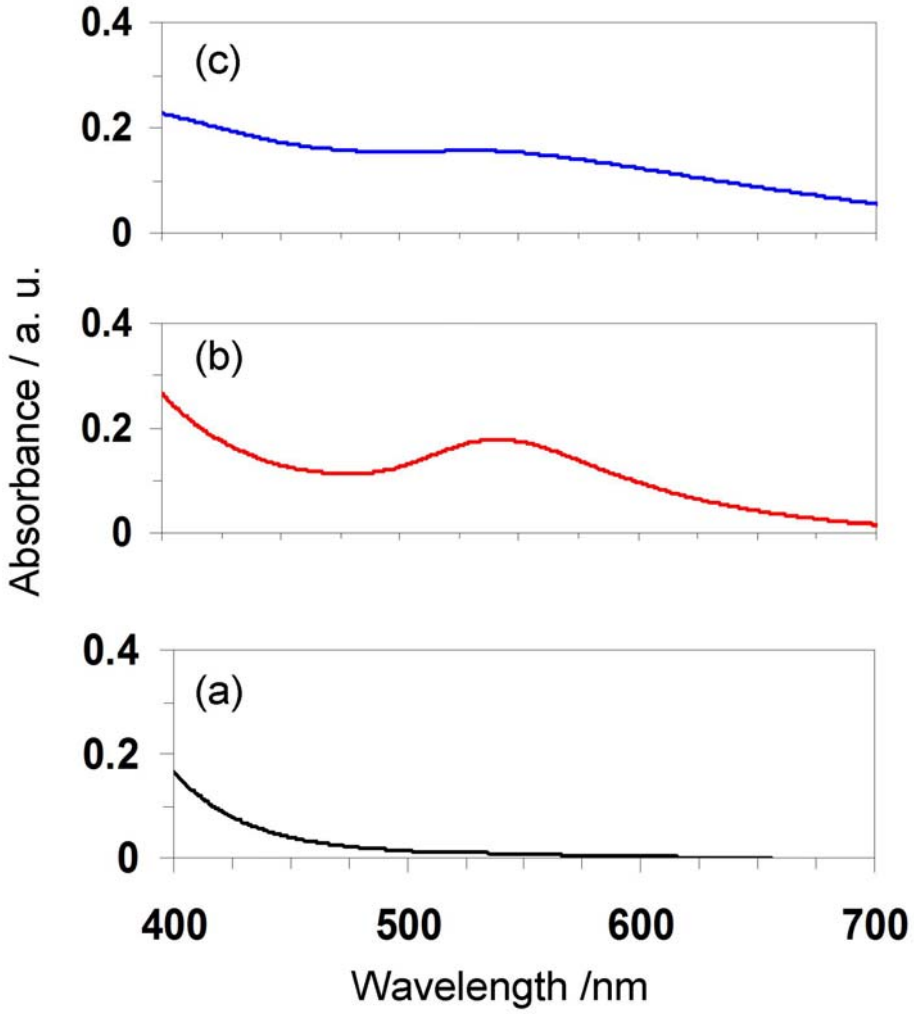

Figure 2.2. UV–Vis spectra during the synthesis of Au/Co/Fe core–shell NPs at reaction times of (a) 0 s, (b) 10 s, and (c) 120 s.

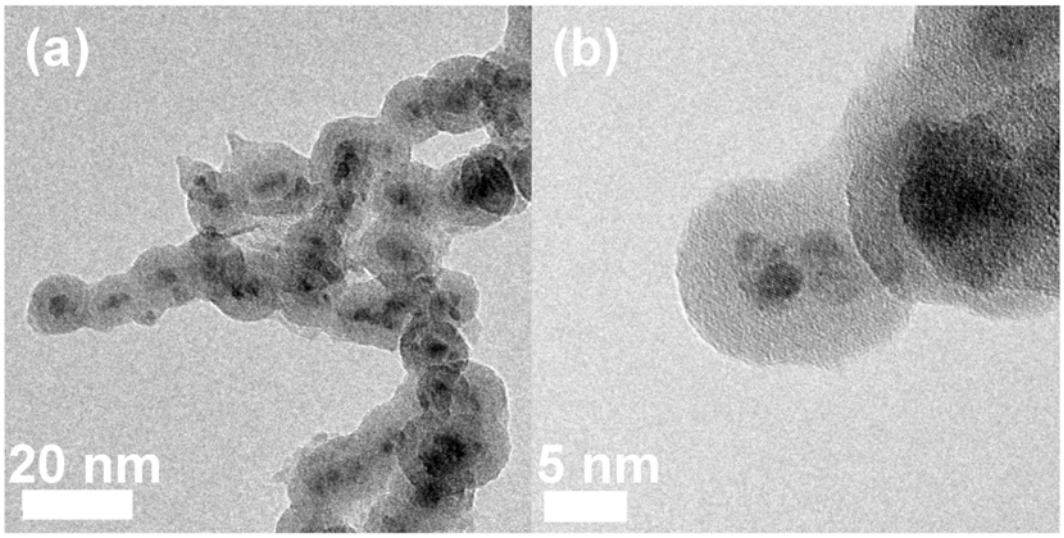

Figure 2.3. TEM images of Au/Co/Fe core–shell NPs with (a) low and (b) high magnification.

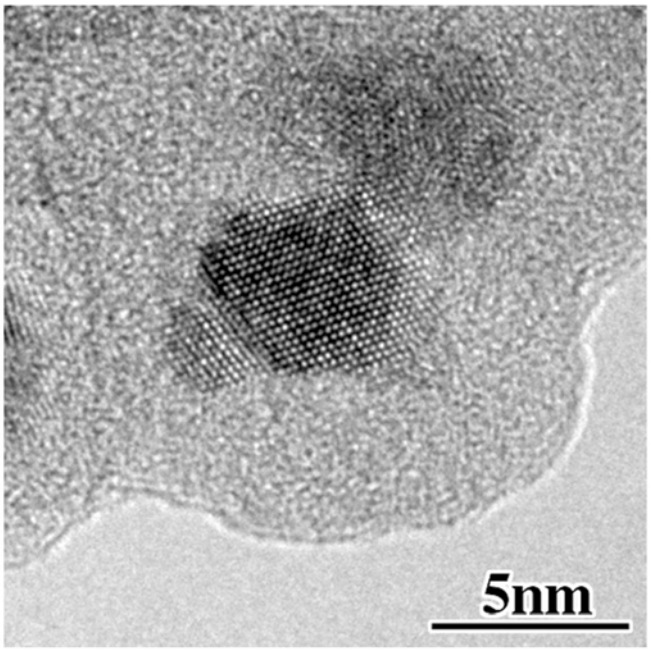

Figure 2.4. High resolution TEM image of the Au core of the Au/Co/Fe core–shell NPs.

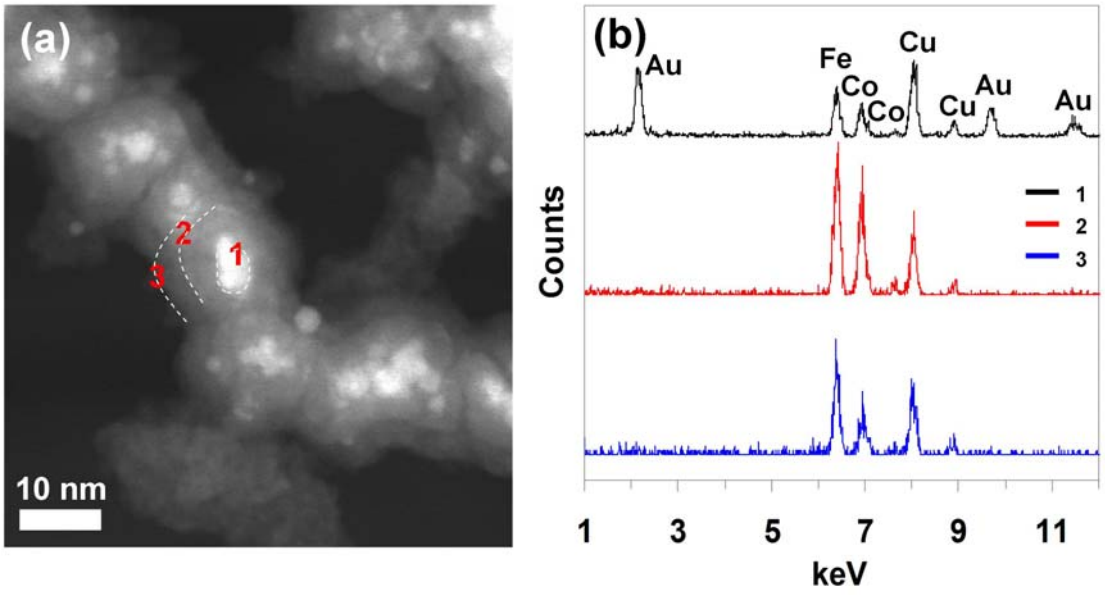

Figure 2.5. (a) HAADF-STEM of Au/Co/Fe triple-layered core–shell NPs. The broken line clearly shows the triple-layered structure. (b) The corresponding EDS spectra at the points indicated in (a).

TEM images of the Au/Co/Fe triple-layered core–shell NPs with different magnification are shown in Figure 2.3. The NPs are roughly spherical in shape and ~10 nm in size. The observed contrast in the NP structure indicates the formation of core, inter-layer, and outer shell layers. High resolution TEM image (Figure 2.4) indicates that the sample consists of a crystalline Au core and amorphous Co and Fe outer layers. An HAADF-STEM image is shown in Figure 2.5a and the corresponding EDS spectra are shown in Figure 2.5b. The EDS analysis reveals the Au:Co:Fe atomic ratio to be 6:6:88, which agrees well with the atomic ratio in the precursors. Only the EDS spectrum at the core part of the NPs (point 1) shows Au peaks, confirming that Au atoms exist only in the center of the NPs. Comparing the EDS spectrum at point 2 with the spectrum at point 3, there is a clear difference in the Co/Fe peak area ratio. The

HAADF-STEM image and corresponding elemental maps obtained by EELS measurements on the Au/Co/Fe triple-layered core–shell NPs also provide clear evidence that the core of the NPs is Au, whilst the inter-layer is Co-rich and the outer shell is Fe-rich (Figure 2.6).

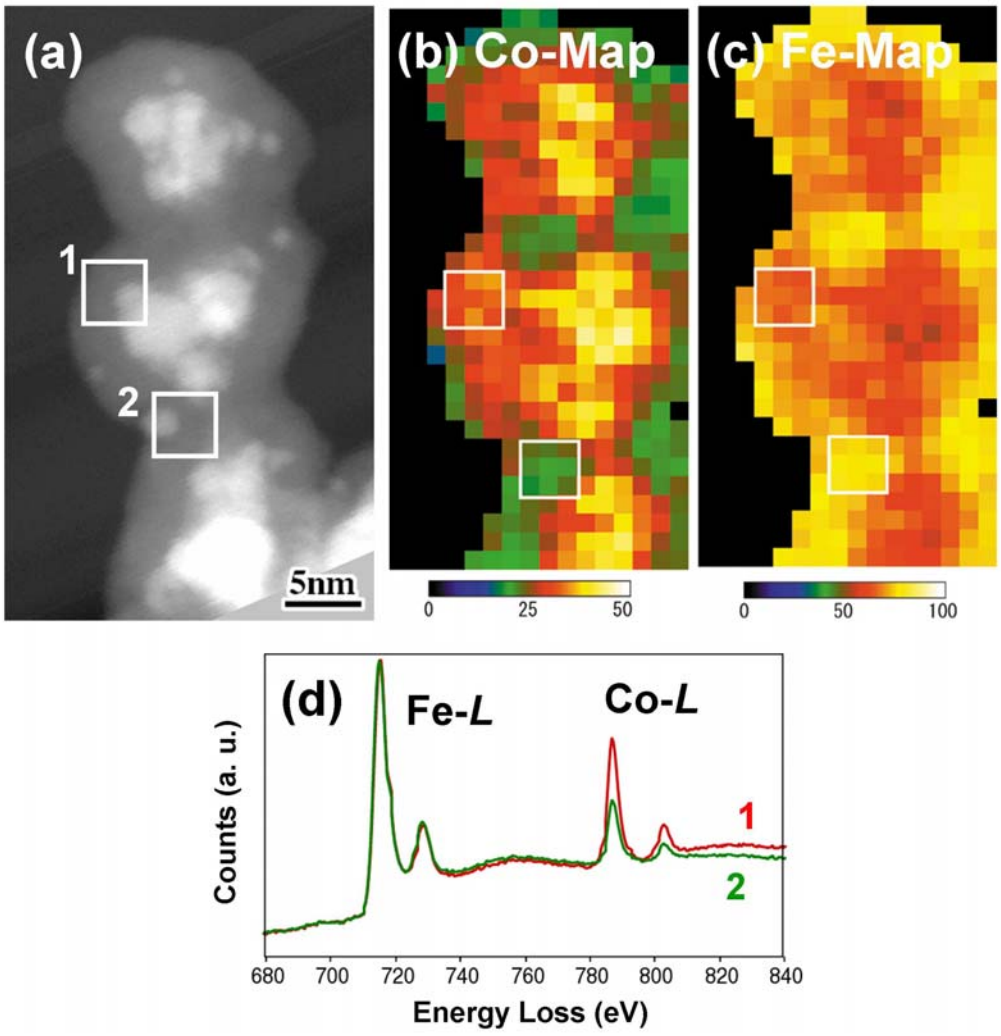

Figure 2.6. (a) HAADF-STEM image of Au/Co/Fe triple-layered core–shell NPs and corresponding elemental maps by EELS for (b) Co and (c) Fe, and (d) the EELS spectra at the areas indicated in (a). The bright parts in (a) show Au cores. The yellow parts in (b) indicate that the inter-layer is Co-rich. The yellow parts in (c) indicate that the outer shell is Fe-rich.

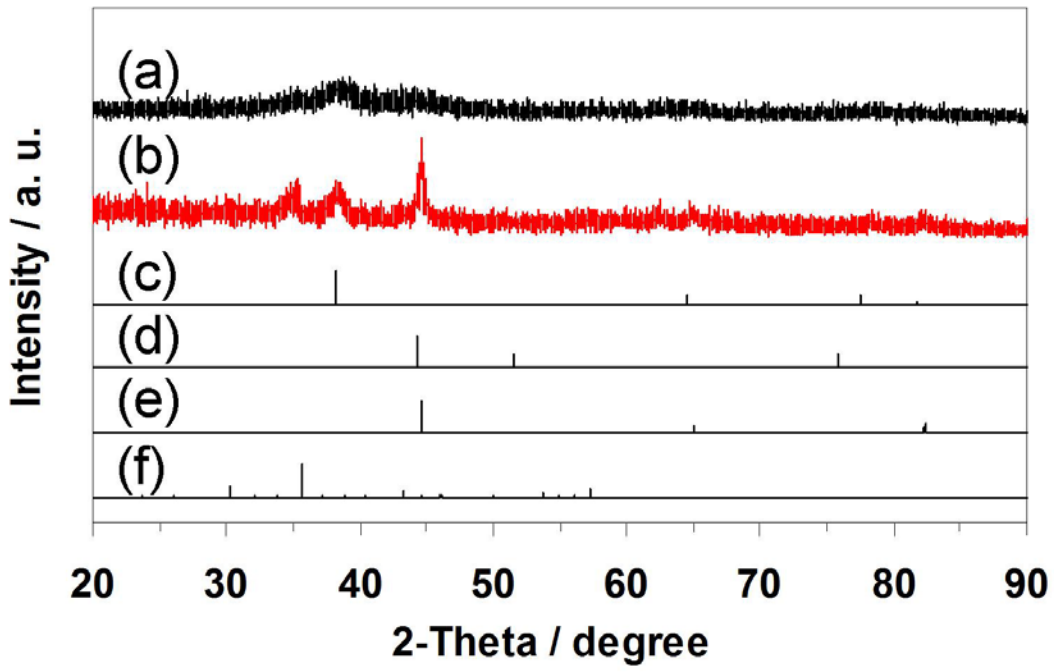

Figure 2.7. XRD patterns of Au/Co/Fe triple-layered core–shell NPs (a) before and (b) after heat treatment at 873 K for 5 h in a He atmosphere. The reference XRD patterns of (c) Au (powder diffraction file (PDF) 65-2870), (d) Co (PDF 15-0806), (e) Fe (PDF 06-0696), and (f) Fe_2O_3 (PDF 39-1346).

Powder XRD patterns of Au/Co/Fe NPs before and after heat treatment at 873 K for 5 h in a He atmosphere are shown in Figure 2.7. After heat treatment, the amorphous Co and Fe outer layers became crystalline metallic Co and Fe (Figure 2.7b). The weak XRD peaks characteristic of Fe_2O_3 might be due to the exposure of the samples to air during the treatment or/and measurements. The TEM and HAADF-STEM results revealed that the most of Au/Co/Fe NPs still retain the triple-layered core–shell structure after heat treatment (Figures 2.8 and 2.9).

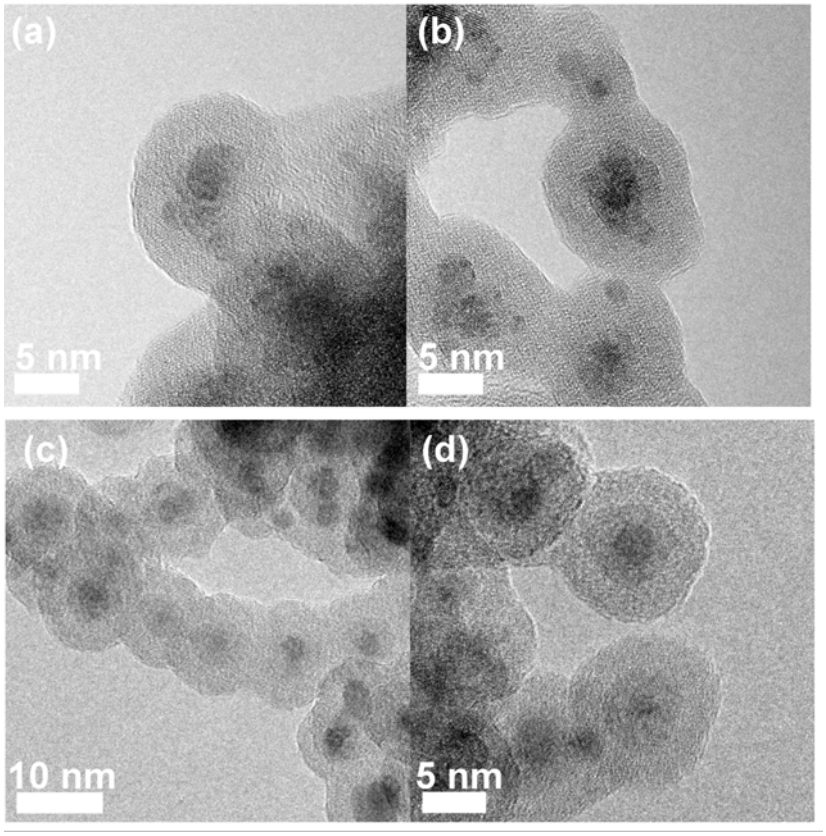

Figure 2.8. High resolution TEM images of (a. b) as-prepared Au/Co/Fe triple-layered core–shell NPs and (c, d) after heat treatment at 873 K in He.

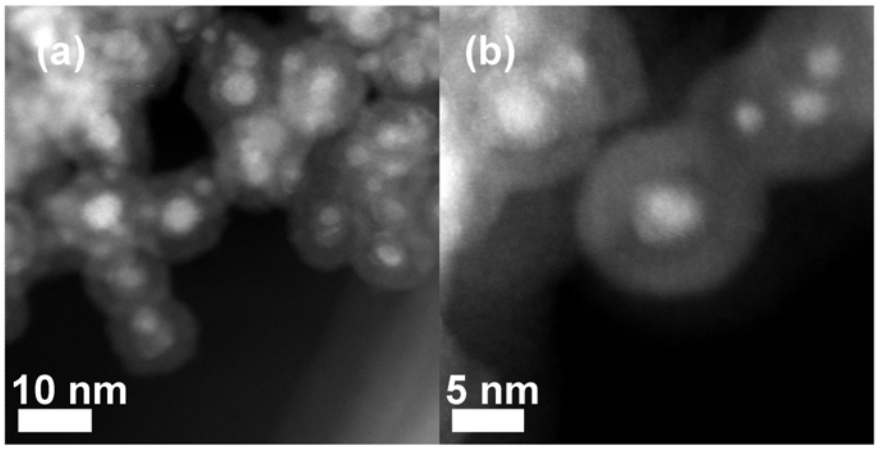

Figure 2.9. HAADF-STEM images of Au/Co/Fe triple-layered core–shell NPs after heat treatment at 873 K in He with (a) low and (b) high magnification.

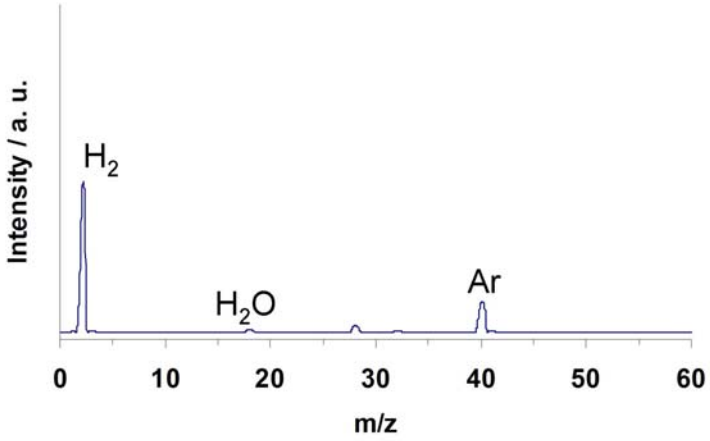

Figure 2.10. Mass spectrum of released gases from aqueous ammonia borane solution (0.17 mol/L, 10.0 mmol) catalyzed by Au/Co/Fe triplelayered core–shell NPs (Au = 0.012 mmol, Co = 0.012 mmol, and Fe = 0.176 mmol) under an argon atmosphere at 298 K. Peaks at *m*/*z* = 28 and 32 are due to N_2 and O_2 impurities from air. Gas phase ammonia (NH_3) and related species were not detected in the mass spectrum.

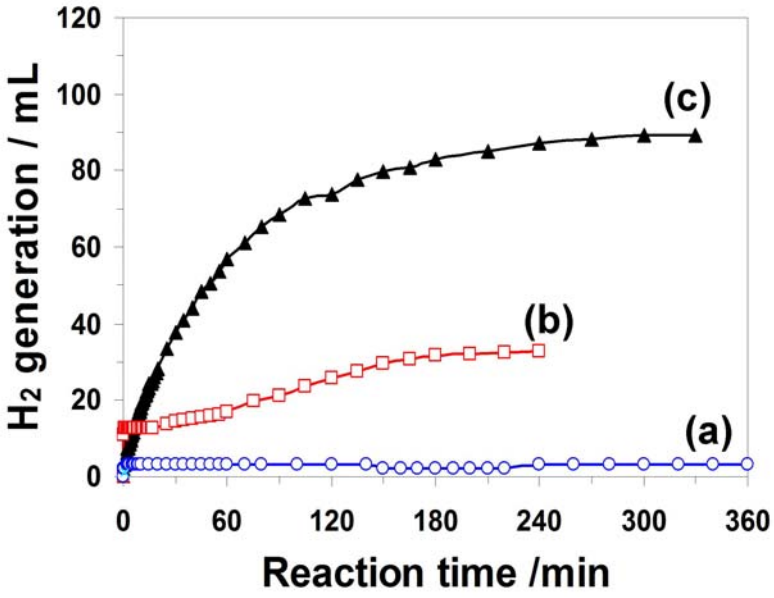

Figure 2.11. Hydrogen generation from aqueous AB solution (0.17 mol/L, 10.0 mL) catalyzed by (a) Co (0.012 mmol), (b) Fe (0.176 mmol), and (c) Au (0.012 mmol) monometallic NPs at room temperature.

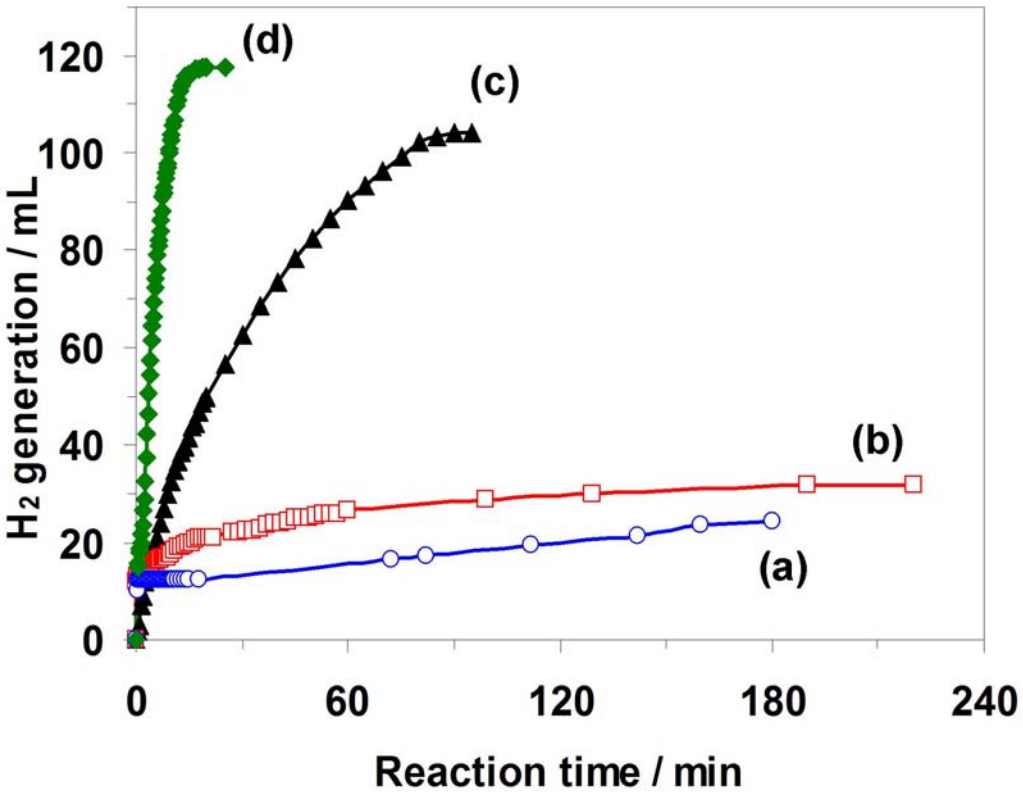

Figure 2.12. Hydrogen generation from aqueous AB solution (0.17 mol/L, 10.0 mL) catalyzed by (a) Co/Fe (Co = 0.012 mmol, Fe = 0.176 mmol), (b) Au/Fe (Au = 0.012 mmol, Fe = 0.176 mmol), (c) Au/Co (Au = 0.012 mmol, Co = 0.012 mmol) bimetallic NPs, and (d) Au/Co/Fe (Au = 0.012 mmol, Co = 0.012 mmol, and Fe = 0.176 mmol) trimetallic core–shell NPs at room temperature.

The catalytic properties of Au/Co/Fe core–shell NPs and those of the monometallic Au, Co, Fe and bimetallic Co/Fe, Au/Fe, Au/Co counterparts were compared using the hydrolytic dehydrogenation of AB as a probe reaction [22–36]. Figure 2.10 shows the mass analysis of the gases generated from the hydrolysis of AB (0.17 mol/L, 10.0 mL) catalyzed by Au/Co/Fe triple-layered core–shell NPs (Au = 0.012 mmol, Co = 0.012 mmol, and Fe = 0.176 mmol) under an argon atmosphere at 298 K. It is obvious that the released gas was pure H_2. Gas phase ammonia (NH_3) and related species were not

detected in the mass spectrum. The catalytic activities of monometallic Au, Co, and Fe catalysts are shown in Figure 2.11. Only 70% of the maximum amount of hydrogen was released after 300 min with Au NP catalysts (Figure 2.11c), and almost no H_2 release was observed with the Co catalyst and only 25% of the maximum amount of H_2 was released with the Fe catalyst in 200 min (Figures 2.11a and 2.11b). These results indicate that the monometallic Co^{2+} and Fe^{3+} cations are not readily reduced by AB to Co and Fe to form active catalysts for AB hydrolytic dehydrogenation.

The catalytic activities of bimetallic Co/Fe, Au/Fe, Au/Co and trimetallic Au/Co/Fe NPs are displayed in Figure 2.12. Both Co/Fe and Au/Fe catalysts (Figsures 2.12a and 2.12b) show catalytic activities similar to that of the monometallic Fe catalyst. The bimetallic Au/Co catalyst shows much better activity (Figure 2.12c), indicating the formation of highly active Au@Co core–shell NPs as reported previously by us [16]: Au^{3+} was readily reduced by AB to yield Au NPs which catalyze the decomposition of AB to generate H_2 and active –H species, which further induce the reduction of Co^{2+} to Co seeds to give Au/Co core–shell NPs, which act as an active catalyst for the hydrolysis of AB [16]. In contrast, bimetallic Au/Fe and Co/Fe NPs show low catalytic activities, similar to that of the monometallic Fe catalyst, indicating that the presence of singlecomponent Au or Co is not sufficient to facilitate the reduction of Fe^{2+}.

In contrast to the observation that the presence of Au alone is not effective in facilitating the reduction of Fe^{2+} and the formation of an active Fe NP catalyst, the co-existence of small amounts of both Au and Co enhanced the reduction of Fe^{2+} and formed a highly active catalyst. As shown in Figure 2.12d, the Au/Co/Fe NPs exhibited the highest activity of all of the catalysts. In the presence of Au^{3+}, Co^{2+}, and Fe^{3+} cations, based on their reduction potentials AB can readily reduce Au^{3+} to Au and Fe^{3+} to Fe^{2+}.

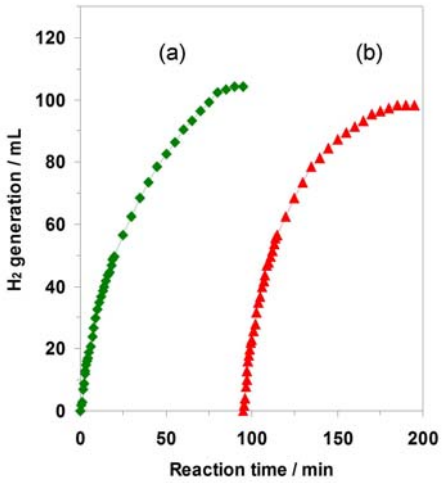

Figure 2.13. (a) Hydrogen generation from aqueous ammonia borane solution (0.17 mol/L, 10.0 mL) catalyzed by Au/Co bimetallic NPs (Au = 0.012 mmol, Co = 0.012 mmol) at room temperature. (b) Hydrogen generation by adding another equivalent amount of ammonia borane into the solution after (a).

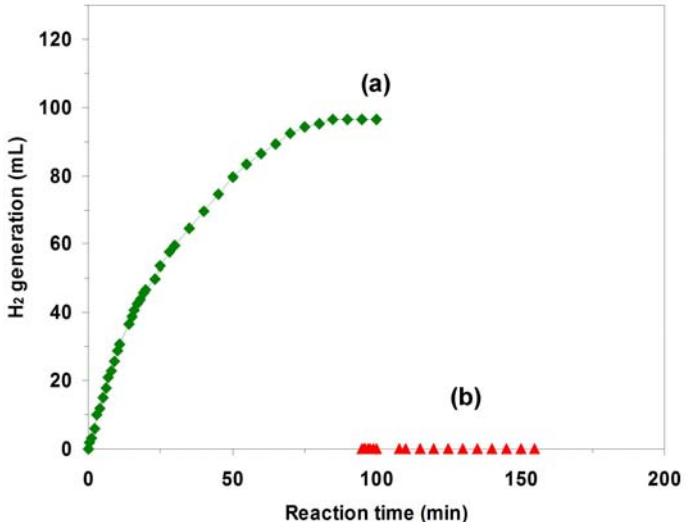

Figure 2.14. (a) Hydrogen generation from aqueous ammonia borane solution (0.17 mol/L, 10.0 mL) catalyzed by Au/Co bimetallic NPs (Au = 0.012 mmol, Co = 0.012 mmol) at room temperature. (b) Hydrogen generation by adding 0.02 mmol PtO_2 into the solution after (a).

The resulting Au seeds catalyze the decomposition of AB to form hydrogen atoms and molecules which reduce Co^{2+} to Co to form the Co-rich layer around the Au core giving the Au/Co bimetallic core–shell NPs. Hydrogen atoms and molecules were rapidly produced due to the high catalytic activity of Au@Co NPs, which further enables the reduction of Fe^{2+} to Fe and the formation of the Fe-rich outer shell.

The theoretical molar ratio of hydrolytically generated hydrogen to AB is 3.0, corresponding to 127 mL H_2 evolution under our reaction conditions. The observed results indicate that the hydrolytic dehydrogenation was complete in the presence of Au/Co/Fe trimetallic core–shell NPs (Figure 2.12d), while in the presence of monometallic Au, Co, and Fe NPs and bimetallic Au/Co, Au/Fe, and Co/Fe NPs, the dehydrogenation was not complete. When a further equivalent amount of AB was added to the solution after the reaction in the presence of Au/Co bimetallic NPs, a further H_2 release of 98 mL was observed, however, as shown in Figure 2.13. This volume is almost the same as that in the first run, indicating that the Au/Co bimetallic NPs retain their catalytic activity during the reaction. Furthermore, when highly active PtO_2 [27] was added to the solution after reaction no hydrogen release was observed (Figure 2.14b), confirming that no unreacted AB was present. These two observations suggest that the incomplete dehydrogenation observed in the presence of the monometallic and bimetallic catalysts may possibly be a result of side-reactions, such as the dehydrogenation of AB (Equations 2.2 and 2.3) [37–39]; these are known to occur in addition to the hydrolysis of AB (as shown by ^{11}B nuclear magnetic resonance (NMR) spectroscopy of the reaction solution in our previous report [12]).

$$NH_3BH_3 \longrightarrow H_2NBH_2 + H_2 \qquad (2.2)$$

$$H_2NBH_2 \longrightarrow HNBH + H_2 \quad (2.3)$$

Smaller amounts of hydrogen (1 or 2 equiv.) are generated via these reactions than via hydrolysis of AB (3 equiv. of hydrogen). It has been observed with many catalysts, for example, palladium black [27], platinum- and nickel-based alloys [40], and gold-, nickel-, and copper-based catalysts [12, 41, 42], that less than a stoichiometric amount of hydrogen is generated, arising from the incomplete hydrolysis of AB.

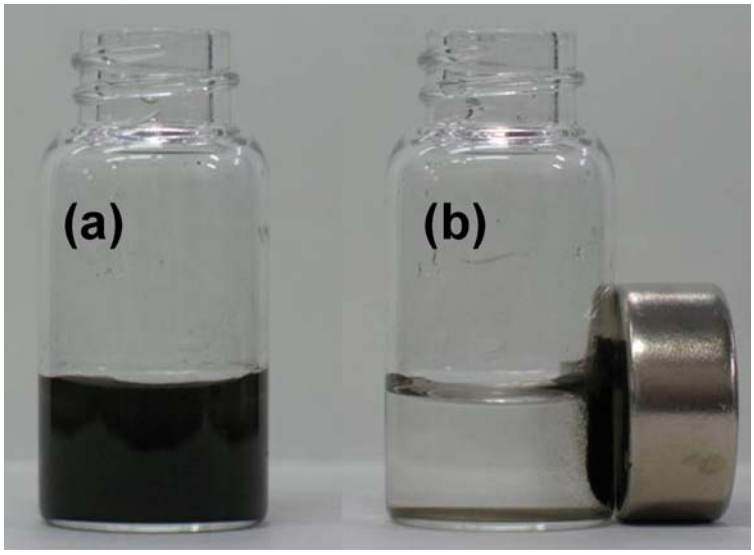

Figure 2.15. Photographs of the Au/Co/Fe core–shell NPs (a) before and (b) after magnetic separation.

High stability and easy recyclability are key requirements for practical catalysts. Magnetic NPs have the advantage of being easily separated by a magnet. During the reaction, the black particles were suspended in the aqueous solution (Figure 2.15a), while after reaction the magnetic particles can be effectively congregated and separated by a magnet (Figure 2.15b). The efficient magnetic separation is very useful for recycling of the catalyst, especially in solution systems.

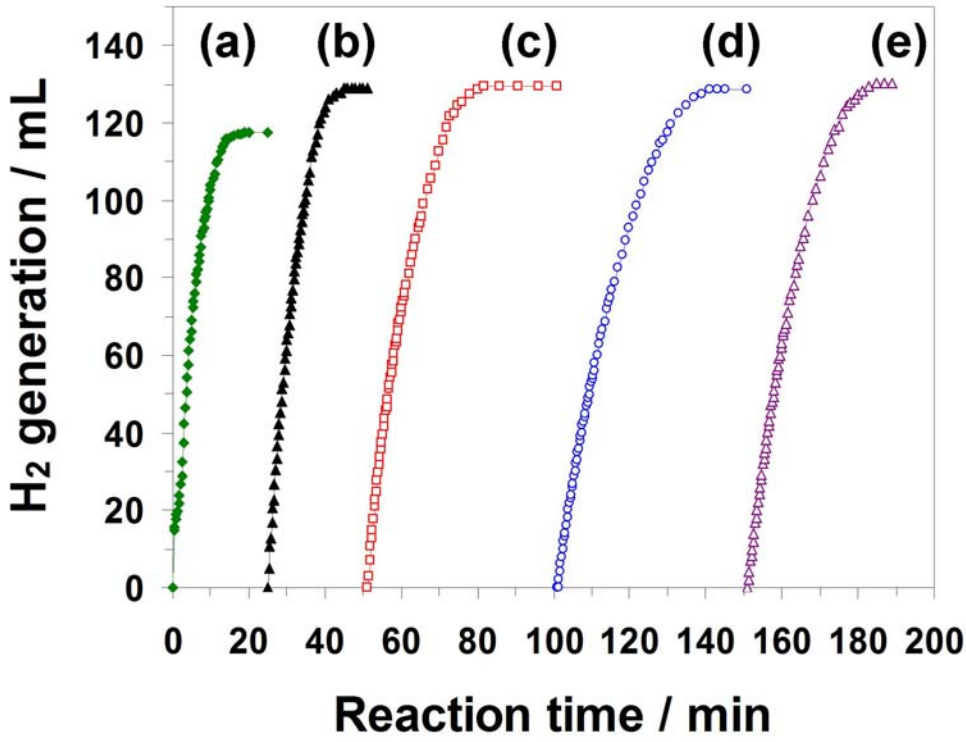

Figure 2.16. Hydrogen generation from aqueous AB solution (0.17 mol/L, 10.0 mL) catalyzed by Au/Co/Fe (Au = 0.012 mmol, Co = 0.012 mmol, and Fe = 0.176 mmol) trimetallic core–shell NPs at room temperature in the (a) 1st, (b) 2nd, (c) 3rd, (d) 4th, and (e) 5th runs carried out by addition of equivalent amounts of AB.

After the hydrogen generation reaction was complete, durability tests of the Au/Co/Fe NPs were conducted using magnetic decantation. Figure 2.16 shows the profiles of hydrogen generation from aqueous AB solution (0.17 mol/L, 10.0 mL) *vs*. reaction time catalyzed by *in situ* synthesized Au/Co/Fe NPs at room temperature over several runs with the addition of additional equivalent amounts of AB. Even after the 5th run, the Au/Co/Fe NPs maintained their initial catalytic activity. The structures and compositions of the reused catalyst were essentially the same as those of the initial material as confirmed by TEM, HAADFSTEM, and EDS measurements (Figures 2.17–2.19).

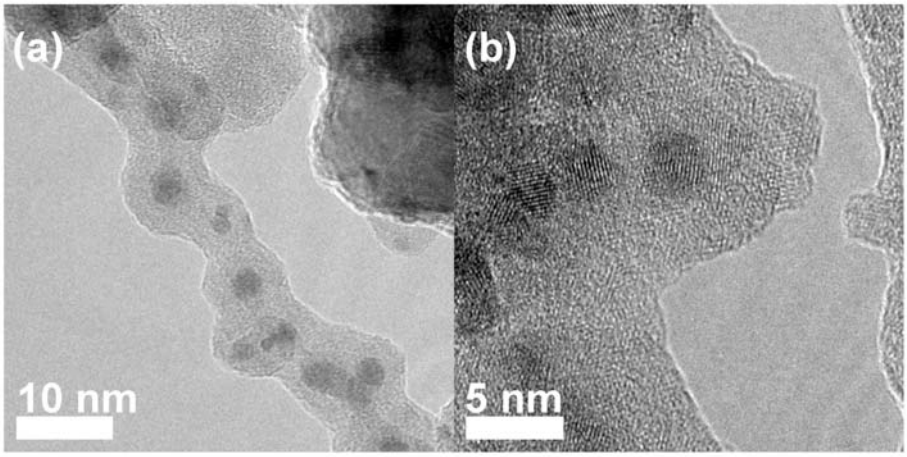

Figure 2.17. TEM images of Au/Co/Fe triple-layered core–shell NPs after the 5th run of ammonia borane hydrolytic dehydrogenation with (a) low and (b) high magnification.

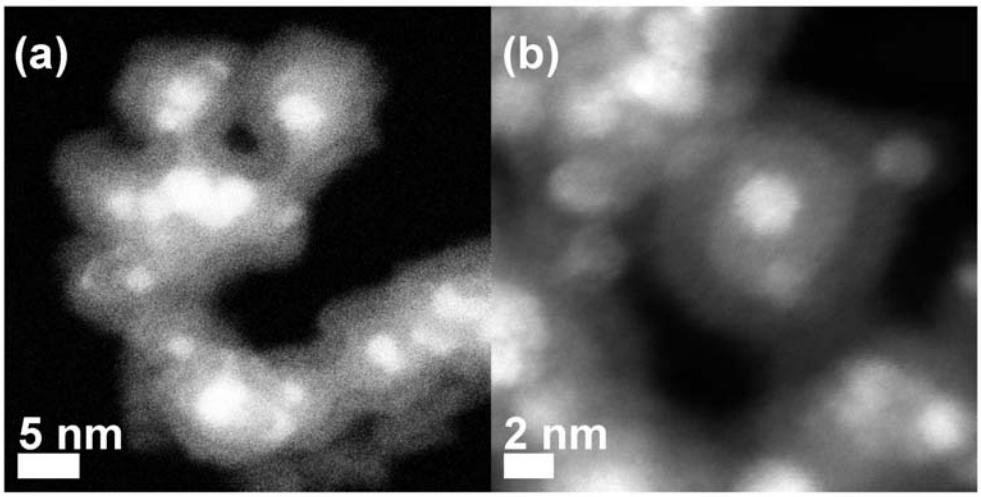

Figure 2.18. HAADF-STEM images of Au/Co/Fe triple-layered core–shell NPs after the 5th run of ammonia borane hydrolytic dehydrogenation with (a) low and (b) high magnification.

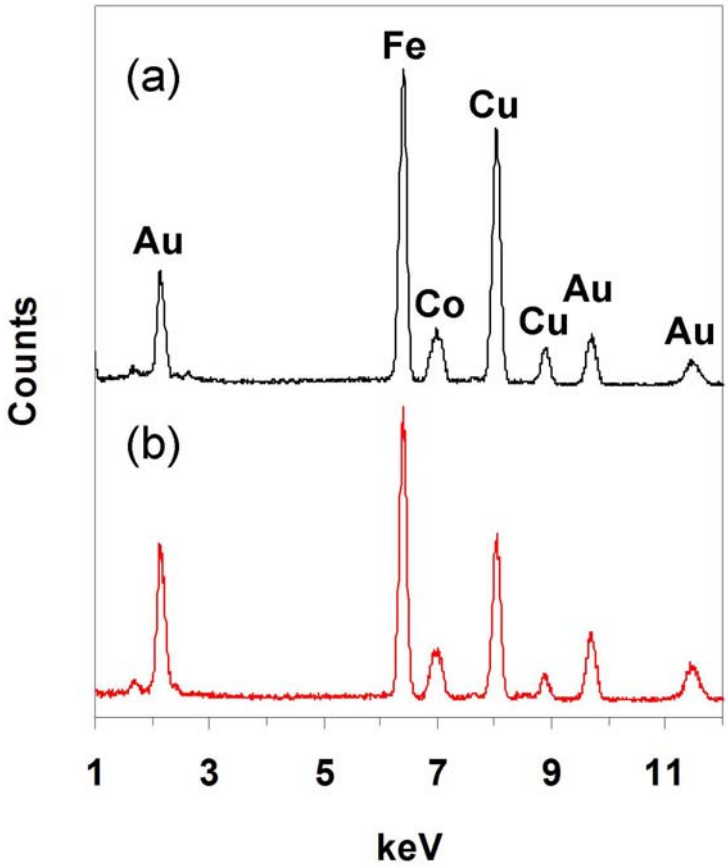

Figure 2.19. EDS spectra of Au/Co/Fe triple-layered core–shell NPs after the (a) 1st and (b) 5th runs of ammonia borane hydrolytic dehydrogenation.

2.4. Conclusion

We have developed the first one-step seeding-growth method for the synthesis of magnetic triple-layered core–shell Au/Co/Fe NPs at room temperature underambient atmosphere. The resulting Au/Co/Fe NPs exhibit much higher catalytic activity for the hydrolytic dehydrogenation of ammonia borane than the corresponding mono- and bi-metallic NPs. This simple technique can be extended to other multi-metallic systems, which should be useful as optical, magnetic, and electrical materials as well as in heterogeneous catalysis.

References

[1] N. Toshima, M. Harada, T. Yonezawa, K. Kushihashi, K. Asakura, *J. Phys. Chem.* **1991**, *95*, 7448–7453.

[2] Y. G. Sun, Y. N. Xia, *Science* **2002**, *298*, 2176–2179.

[3] N. Toshima, M. Kanemaru, Y. Shiraishi, Y. Koga, *J. Phys. Chem. B* **2005**, *109*, 16326–16331.

[4] O. M. Wilson, R. W. J. Scott, J. C. Garcia-Martinez, R. M. Crooks, *J. Am. Chem. Soc.* **2005**, *127*, 1015–1024.

[5] F. Tao, M. E. Grass, Y. W. Zhang, D. R. Butcher, J. R. Renzas, Z. Liu, J. Y. Chung, B. S. Mun, M. Salmeron, G. A. Somorjai, *Science* **2008**, *322*, 932–934.

[6] S. Alayoglu, A. U. Nilekar, M. Mavrikakis, B. Eichhorn, *Nat. Mater.* **2008**, *7*, 333–338.

[7] J. Yang, E. H. Sargent, S. O. Kelley, J. Y. Ying, *Nat. Mater.* **2009**, *8*, 683–689.

[8] Y. W. Lee, M. Kim, Z. H. Kim, S. W. Han, *J. Am. Chem. Soc.* **2009**, *131*, 17036–17037.

[9] H. Kobayashi, M. Yamauchi, H. Kitagawa, Y. Kubota, K. Kato, M. Takata, *J. Am. Chem. Soc.* **2010**, *132*, 5576–5577.

[10] R. Ferrando, J. Jellinek, R. L. Johnston, *Chem. Rev.* **2008**, *108*, 845–910.

[11] Z. Y. Zhang, T. M. Nenoff, K. Leung, S. R. Ferreira, J. Y. Huang, D. T. Berry, P. P. Provencio, R. Stumpft, *J. Phys. Chem. C* **2010**, *114*, 14309–14318.

[12] H. L. Jiang, T. Umegaki, T. Akita, X. B. Zhang, M. Haruta, Q. Xu, *Chem. Eur. J.* **2010**, *16*, 3132–3137.

[13] D. S. Wang, Y. D. Li, *J. Am. Chem. Soc.* **2010**, *132*, 6280–6281.

[14] H. L. Jiang, T. Akita, T. Ishida, M. Haruta, Q. Xu, *J. Am. Chem. Soc.* **2011**, *133*, 1304–1306.

[15] J. M. Yan, X. B. Zhang, S. Han, H. Shioyama, Q. Xu, *J. Power Sources* **2009**, *194*, 478–481.

[16] J. M. Yan, X. B. Zhang, T. Akita, M. Haruta, Q. Xu, *J. Am. Chem. Soc.* **2010**, *132*, 5326–5327.

[17] V. Mazumder, M. F. Chi, K. L. More, S. H. Sun, *J. Am. Chem. Soc.* **2010**, *132*, 7848–7849.

[18] N. Toshima, R. Ito, T. Matsushita, Y. Shiraishi, *Catal. Today* **2007**, *122*, 239–244.

[19] V. Mazumder, M. F. Chi, K. L. More, S. H. Sun, *Angew. Chem. Int. Ed.* **2010**, *49*, 9368–9372.

[20] L. Wang, Y. Yamauchi, *J. Am. Chem. Soc.* **2010**, *132*, 13636–13638.

[21] J. R. Kitchin, J. K. Nørskov, M. A. Barteau, J. G. Chen, *Phys. Rev. Lett.* **2004**, *93*, 156801.

[22] C. W. Hamilton, R. T. Baker, A. Staubitz, I. Manners, *Chem. Soc. Rev.* **2009**, *38*, 279–293.

[23] A. Gutowska, L. Y. Li, Y. S. Shin, C. M. M. Wang, X. H. S. Li, J. C. Linehan, R. S. Smith, B. D. Kay, B. Schmid, W. Shaw, M. Gutowski, T. Autrey, *Angew. Chem. Int. Ed.* **2005**, *44*, 3578–3582.

[24] M. E. Bluhm, M. G. Bradley, R. Butterick, U. Kusari, L. G. Sneddon, *J. Am. Chem. Soc.* **2006**, *128*, 7748–7749.

[25] H. V. K. Diyabalanage, R. P. Shrestha, T. A. Semelsberger, B. L. Scott, M. E. Bowden, B. L. Davis, A. K. Burrell, *Angew. Chem. Int. Ed.* **2007**, *46*, 8995–8997.

[26] Z. T. Xiong, C. K. Yong, G. T. Wu, P. Chen, W. Shaw, A. Karkamkar, T. Autrey,

M. O. Jones, S. R. Johnson, P. P. Edwards, W. I. F. David, *Nat. Mater.* **2008**, *7*, 138–141.

[27] M. Chandra, Q. Xu, *J. Power Sources* **2006**, *156*, 190–194.

[28] Q. Xu, M. Chandra, *J. Power Sources* **2006**, *163*, 364–370.

[29] Q. Xu, M. Chandra, *J. Alloys. Compd.* **2007**, *446*, 729–732.

[30] J. M. Yan, X. B. Zhang, S. Han, H. Shioyama, Q. Xu, *Angew. Chem. Int. Ed.* **2008**, *47*, 2287–2289.

[31] T. Umegaki, J. M. Yan, X. B. Zhang, H. Shioyama, N. Kuriyama, Q. Xu, *Int. J. Hydrogen Energy* **2009**, *34*, 2303–2311.

[32] H. L. Jiang, S. K. Singh, J. M. Yan, X. B. Zhang, Q. Xu, *ChemSusChem* **2010**, *3*, 541–549.

[33] Ö. Metin, V. Mazumder, S. Özkar, S. S. Sun, *J. Am. Chem. Soc.* **2010**, *132*, 1468–1469.

[34] S. Çalışkan, M. Zahmakıran, S. Özkar, *Appl. Catal. B-Environ.* **2010**, *93*, 387–394.

[35] U. B. Demirci, P. Miele, *J. Power Sources* **2010**, *195*, 4030–4035.

[36] H. L. Jiang, Q. Xu, *Catal. Today* **2011**, *170*, 56–63.

[37] M. C. Denney, V. Pons, T. J. Hebden, D. M. Heinekey, K. I. Goldberg, *J. Am. Chem. Soc.* **2006**, *128*, 12048–12049.

[38] R. J. Keaton, J. M. Blacquiere, R. T. Baker, *J. Am. Chem. Soc.* **2007**, *129*, 1844–1845.

[39] F. H. Stephens, V. Pons, R. T. Baker, *Dalton Trans.* **2007**, 2613–2626.

[40] C. F. Yao, L. Zhuang, Y. L. Cao, X. P. Ai, H. X. Yang, *Int. J. Hydrogen Energy* **2008**, *33*, 2462–2467.

[41] S. B. Kalidindi, U. Sanyal, B. R. Jagirdar, *Phys. Chem. Chem. Phys.* **2008**, *10*,

5870–5874.

[42] T. Umegaki, J. M. Yan, X. B. Zhang, H. Shioyama, N. Kuriyama, Q. Xu, *J. Power Sources* **2009**, *191*, 209–216.

Chapter 3

Dendrimer-encapsulated bimetallic Pt-Ni nanoparticles as highly efficient catalysts for hydrogen generation from chemical hydrogen storage materials

3.1. Introduction

Dendrimers, which have highly branched structures, are very important for the encapsulation of metal salts and the formation of nanoparticles (NPs) and clusters of desired sizes [1–4]. Recently, hydroxyl-terminated poly(amidoamine) (PAMAM) dendrimers have been used extensively as a macroligand to stabilize metallic NPs of different sizes [5–8]. PAMAM dendrimers act as a flexible membrane around metallic NPs, and the application of PAMAM dendrimer-encapsulated NPs (DENs) in catalytic reactions offers promising new opportunities to create tailored catalytic systems [9–14]. Dendrimers offer the control of the number of metal complexes in an assembly through stepwise complexation, which allows the complexes to accumulate in discrete nanocages [15–17].

A great deal of work has been devoted to the development of effective hydrogen storage materials for hydrogen fuel cells and hydrogen-based energy systems [18–22]. Recently, our work has suggested that hydrous hydrazine (*e.g.*, $H_2NNH_2{\cdot}H_2O$) is a promising hydrogen storage material because it is a liquid over a wide temperature range (213–392 K) and contains as much as 8 wt% hydrogen available for hydrogen generation, which can be released by the complete decomposition of hydrazine to

hydrogen and nitrogen (Equation 3.1) [23–32].

$$H_2NNH_2 \longrightarrow N_2 + 2H_2 \quad (3.1)$$

The only byproduct of this reaction (N_2) does not need to be collected for recycling. Moreover, N_2 can be transformed into ammonia by the Haber-Bosch process, homogeneous catalytic processes, or an electrolytic process [33–36] and subsequently to hydrazine on a large scale [37–39] or perhaps transformed directly to hydrazine by using an electrolytic process similar to that for ammonia synthesis [35]. However, the key to effectively exploit the hydrogen storage properties of hydrazine is to avoid its incomplete decomposition by the undesired reaction pathway shown in Equation 3.2.

$$3H_2NNH_2 \longrightarrow N_2 + 4NH_3 \quad (3.2)$$

A number of metal catalysts have been investigated for the decomposition of hydrazine, and the reaction pathways for hydrazine decomposition strongly depend on the catalyst used and the reaction conditions [23–32]. However, the development of highly active and efficient catalysts is of significant importance for the practical use of hydrous hydrazine as a potential hydrogen storage material [23–32].

Another attractive candidate for chemical hydrogen storage is ammonia borane (NH_3BH_3, AB), which has a hydrogen capacity as high as 19.6 wt%, exceeding that of gasoline [40–46]. Hydrogen can be generated by the thermal decomposition of AB [40], and catalytic hydrolysis provides an alternative route for hydrogen generation under milder conditions (Equation 3.3) [41–46].

$$NH_3BH_3 + 2H_2O \longrightarrow NH_4^+ + BO_2^- + 3H_2 \quad (3.3)$$

In this work, we have prepared Pt-Ni DENs with different Pt/Ni ratios by the

co-complexation of Pt^{2+} and Ni^{2+} cations to the internal tertiary amine of fourth-generation hydroxyl-terminated PAMAM dendrimers (G4-OH) followed by coreduction by $NaBH_4$ and investigated their catalytic performances for hydrogen generation from the complete decomposition of hydrous hydrazine and the hydrolysis of AB (Scheme 3.1).

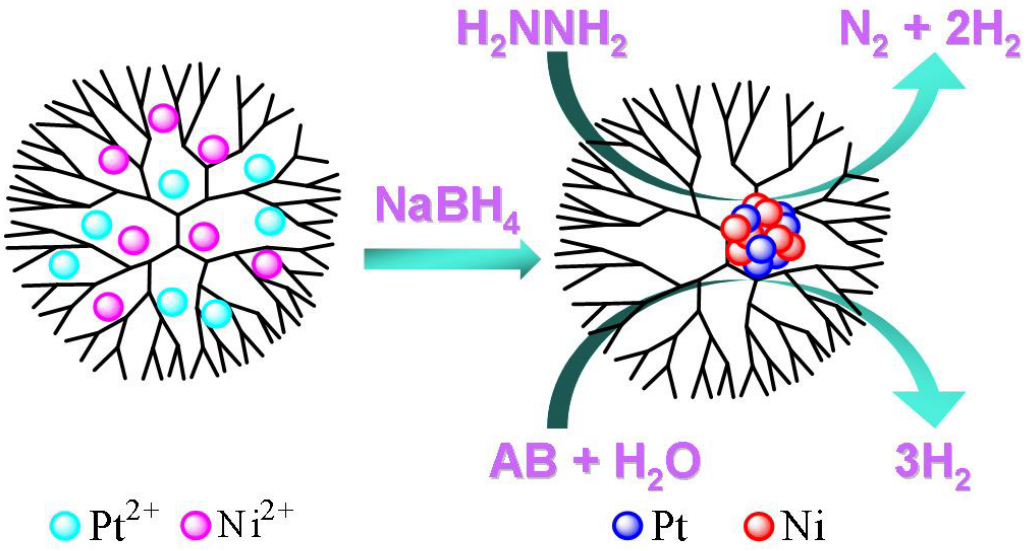

Scheme 3.1. Synthesis of dendrimer-encapsulated Pt-Ni nanoparticles and their use as catalysts for the decomposition of hydrous hydrazine and hydrolysis of AB.

3.2. Experimental details

3.2.1. Chemicals

Commercial chemicals were used as received for catalyst preparation and the catalytic reactions. Ammonia borane (AB, 97%) was purchased from JSC Aviabor. Hydrazine monohydrate (98%), $NaBH_4$ (98.5%), and fourth-generation

hydroxyl-terminated PAMAM dendrimers (G4-OH, 10 wt% in methanol, Mw=14 279) were purchased from Sigma–Aldrich. $NiCl_2 \cdot 6H_2O$ (98.0%) and NaOH (98%) were purchased from Kishida Chemical. K_2PtCl_4 (46.8 ± 0.1% Pt) was purchased from Mitsuwa Chemicals. Deionized H_2O with a specific resistance of 17.5 MΩ cm was obtained by reversed osmosis followed by ion-exchange and filtration (RFD250NB, Toyo Roshi Kaisha, Ltd., Japan).

3.2.2. Syntheses of dendrimer-encapsulated Pt-Ni nanoparticles

Pt-Ni DENs were prepared according to a procedure reported by Crooks and co-workers [9, 16]. Briefly, an aqueous solution that contained K_2PtCl_4 and $NiCl_2 \cdot 6H_2O$ was added to an aqueous solution of G4-OH (0.336 mm, 5 mL), which was prepared in advance by drying to remove methanol from the solution. The metal-to-dendrimer molar ratio was fixed at 60:1 and the Pt/Ni molar ratio was adjusted to x:(60–x) in which x = 60, 48, 36, 24, 12, 6, and 0. The metal complex and dendrimer solution was stirred for 72 h in a 30 mL two-necked round-bottomed flask to allow the Pt^{2+} and Ni^{2+} ions to fully complex with the interior amines of the dendrimers. $NaBH_4$ (20 mg) and hydrazine monohydrate (1.0 mmol) were added to the solution with vigorous shaking, which caused the color of the solution to change from pale yellow to black. The resulting bimetallic G4-OH(Pt_xNi_{60-x}) DENs were characterized and used for the catalytic reactions.

3.2.3. Catalytic reaction of hydrous hydrazine decomposition

The catalytic decomposition of hydrous hydrazine was performed according to our procedure reported previously [23–30]. Typically, $H_2NNH_2 \cdot H_2O$ (1.0 mmol) was injected to a glass reactor that contained an aqueous suspension of Pt-Ni DENs and

NaOH (0.4 M) to initiate the catalytic decomposition reaction of hydrous hydrazine. The reaction temperature was kept at 343 K by using a water bath. The gas released during the reaction was passed through a HCl solution (1.0 M) before it was measured volumetrically. Recently, we reported that the catalytic performance for the decomposition of hydrous hydrazine is strongly dependent on the reaction temperature and the presence of a strong base (NaOH) [27–29]. In this work, we employed reaction conditions similar to those used for Ni-Fe nanocatalysts (0.4 M NaOH, 343 K) [29]. For the preparation of samples for MS, the HCl trap was not used. The selectivity toward H_2 generation (y) was evaluated by using Equation 3.4 [23].

$$3H_2NNH_2 \longrightarrow 4(1-y)NH_3 + 6yH_2 + (1+2y)N_2 \quad (3.4)$$

As NH_3 was absorbed by the water and HCl trap, the gas volume measured at the end of the reaction contained only N_2 and H_2, from which the molar ratio of $n(N_2+H_2)/n(N_2H_4)$ (λ) was obtained. Therefore, the selectivity was calculated by using Equation 3.5:

$$y = (3\lambda-1)/8 \quad (3.5)$$

in which $\lambda = n(N_2+H_2)/n(H_2NNH_2)$ ($1/3 \leq \lambda \leq 3$).

3.2.4. Catalytic reaction of AB hydrolysis

The catalytic hydrolysis of AB was performed following our procedure reported previously [41–43]. Typically, AB (51.5 mg) dissolved in water (1 mL) was injected to a glass reactor that contained an aqueous suspension of Pt-Ni DENs to initiate the hydrolysis of AB. The reaction was performed at room temperature in air. The evolution of H_2 was monitored by using a gas burette.

3.2.5. Catalyst characterization

Ultraviolet-visible (UV–Vis) absorption spectra were recorded by using a Shimadzu UV-2550 spectrophotometer in the wavelength range of 190–600 nm. Transmission electron microscope (TEM, FEI TECNAI G2), high-angle annular dark-field scanning TEM (HAADF-STEM), scanning electron microscope (SEM, Hitachi S-5000), and energy-dispersive X-ray spectroscopy (EDS) were used to determine the detailed microstructure of the Pt-Ni DENs. The TEM (HAADF-STEM, EDS) and SEM samples were prepared by depositing one or two droplets of the NPs suspended in a solution onto amorphous carbon-coated Cu grids, which were then dried under Ar. Mass spectra of the generated gases were collected by using a Balzers Prisma QMS 200 mass spectrometer. X-ray photoelectron spectroscopy (XPS) analysis was carried out on a Shimadzu ESCA-3400 X-ray photoelectron spectrometer using an Mg K source (10 kV, 10 mA). The Ar sputtering experiments were carried out under the conditions of background vacuum 3.4 x 10^{-6} Pa, sputtering acceleration voltage of 2 kV and sputtering current of 10 mA.

3.3. Results and discussion

3.3.1. Catalytic decomposition of hydrous hydrazine

The catalytic decomposition of hydrous hydrazine to hydrogen has been performed over G4-OH(Pt_xNi_{60-x}) DEN catalysts (x = 60, 48, 36, 24, 12, 6, and 0) at 343 K in the presence of NaOH (0.4 M). The catalytic activities and hydrogen selectivities of the G4-OH(Pt_xNi_{60-x}) DENs depend on the Pt/Ni ratio (Figure 3.1).

Monometallic G4-OH(Pt_{60}) DENs are catalytically inactive (Figure 3.1a), and

G4-OH(Ni_{60}) DENs show a poor activity and low hydrogen selectivity (18%; Figure 3.1g) for hydrazine decomposition in aqueous solution. These observations are in agreement with our previous report on the decomposition of hydrous hydrazine with monometallic Pt and Ni catalysts, which show no activity and poor activity, respectively [25]. However, bimetallic Pt-Ni DENs exhibit high catalytic activities and hydrogen selectivities for this reaction. Among the bimetallic DENs investigated, G4-OH($Pt_{12}Ni_{48}$) DENs show the highest activity, and the reaction reached completion in 5 min (metal/H_2NNH_2 = 0.1) with (N_2+H_2)/H_2NNH_2 = 3.0, which corresponds to 100% hydrogen selectivity (Figure 3.1e). The turnover frequency (TOF) for the catalytic decomposition reaction of hydrazine in aqueous solution at 343 K for G4-OH($Pt_{12}Ni_{48}$) is 4.0 $mol_{H_2}\ mol_{metal}^{-1}\ min^{-1}$, which is 14 times the value of Pt-Ni alloy NPs stabilized by hexadecyltrimethylammonium bromide (CTAB) at 333 K [27]. This result indicates that for the catalytic decomposition of hydrous hydrazine, the activity of G4-OH($Pt_{12}Ni_{48}$) DENs is much higher than that of CTAB-stabilized Pt-Ni alloy NPs, which is because of the controlled size of the encapsulated Pt-Ni NPs in dendrimers (see below). Moreover, the TOF value for G4-OH($Pt_{12}Ni_{48}$) is among the highest for hydrous hydrazine decomposition catalysts reported to date [24–32].

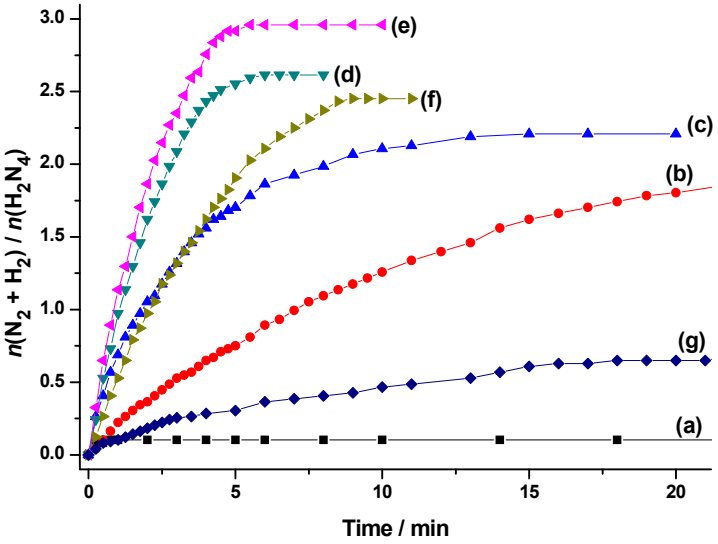

Figure 3.1. Decomposition of hydrous hydrazine (0.2 M; n = moles) to H_2 over time in the presence of G4-OH(Pt_xNi_{60-x}) DENs, x = (a) 60, (b) 48, (c) 36, (d) 24, (e) 12, (f) 6, and (g) 0, with NaOH (0.4 M) at 343 K (metal/H_2NNH_2 = 0.1).

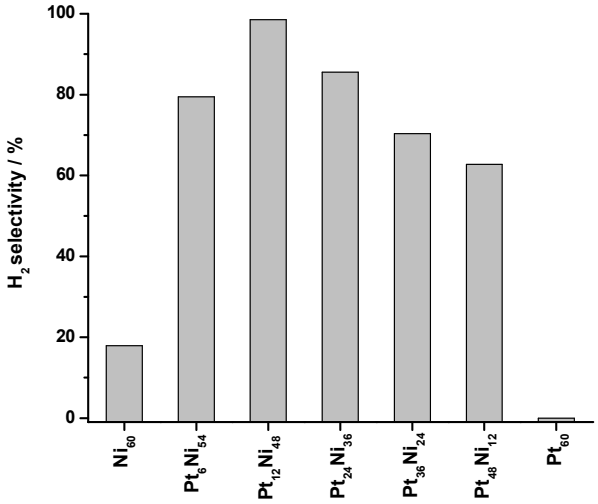

Figure 3.2. H_2 selectivities in the decomposition of hydrous hydrazine (0.2 M) to H_2 in the presence of G4-OH(Pt_xNi_{60-x}) DENs, x = 60, 48, 36, 24, 12, 6, and 0, with NaOH (0.4 M) at 343 K (metal/H_2NNH_2 = 0.1).

G4-OH($Pt_{12}Ni_{48}$) DENs exhibit a 100% hydrogen selectivity, whereas the other bimetallic Pt-Ni DENs (G4-OH(Pt_6Ni_{54}), 79%; G4-OH($Pt_{24}Ni_{36}$), 86%; G4-OH($Pt_{36}Ni_{24}$), 70%; G4-OH($Pt_{48}Ni_{12}$), 63%) and monometallic Ni DENs (G4-OH(Ni_{60}), 18%) show lower hydrogen selectivities, and G4-OH(Pt_{60}) DENs are inactive (Figure 3.2). These results indicate the involvement of the bimetallic phase as the active species on the catalyst surface and that the synergistic interaction between Ni and Pt [47] is necessary for the selective decomposition of hydrazine to hydrogen and nitrogen, which is consistent with our previous work [25]. In addition to the volumetric results, the complete decomposition of hydrazine to hydrogen and nitrogen over the bimetallic G4-OH($Pt_{12}Ni_{48}$) DENs has been further confirmed by MS (absence of NH_3 peak; Figure 3.3).

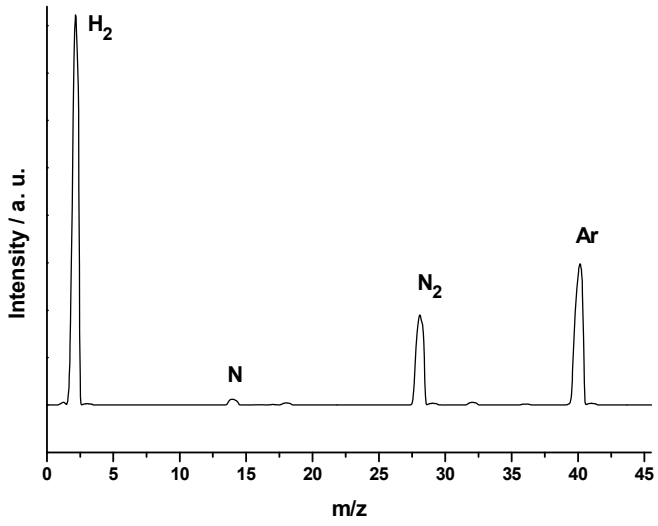

Figure 3.3. Mass spectrum of gases released from the decomposition of hydrous hydrazine (0.2 M) over the G4-OH($Pt_{12}Ni_{48}$) DENs with NaOH (0.4 M) under Ar at 343 K.

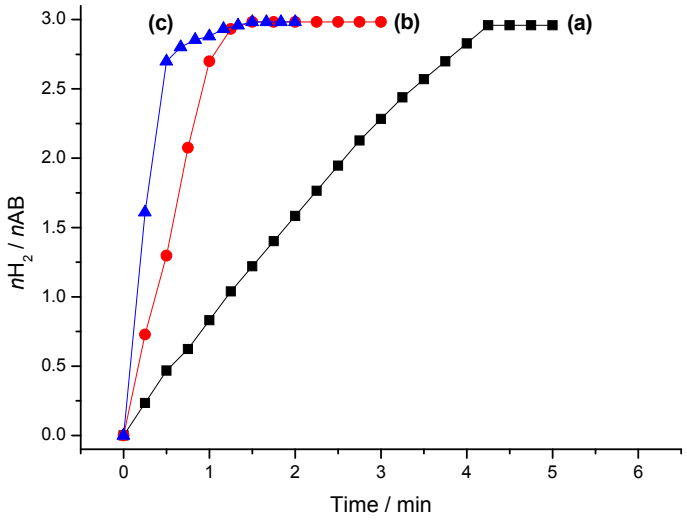

Figure 3.4. H_2 generation from an aqueous AB solution (0.32 M; n = moles) catalyzed by (a) G4-OH(Ni_{60}), (b) G4-OH($Pt_{12}Ni_{48}$), and (c) G4OH(Pt_{60}) DENs at room temperature (metal/AB = 0.062).

3.3.2. Catalytic hydrolysis of ammonia borane

The catalytic activities for the hydrolysis of AB were investigated over the G4-OH(Pt_xNi_{60-x}) DENs at room temperature. Both monometallic Pt and Ni DENs and bimetallic Pt-Ni DENs catalyze AB hydrolysis at room temperature with the release of 3.0 equivalents of hydrogen (Figure 3.4), which indicates complete hydrogen generation from AB according to Equation 3.3. The catalytic AB hydrolysis reactions were completed in 1.0, 1.5, and 4.3 min, which corresponds to TOF values of 48, 32, and 11 mol_{H_2} mol metal^{-1} min^{-1} over G4-OH(Pt_{60}), G4-OH($Pt_{12}Ni_{48}$), and G4-OH(Ni_{60}) DENs, respectively (metal/AB = 0.062). Although the TOF of G4-OH(Pt_{60}) DENs is slightly higher than that of G4-OH($Pt_{12}Ni_{48}$) DENs, the latter contains only 20% Pt instead of 100% Pt in the former. Additionally, the TOF of G4-OH($Pt_{12}Ni_{48}$) DENs is

approximately 6 and 1.5 times higher than that of Pt-Ni catalysts reported previously ($Pt_{12}Ni_{88}$ and $Pt_{65}Ni_{35}$, respectively) [48, 49]. This indicates that the high performances of bimetallic G4-OH($Pt_{12}Ni_{48}$) DENs are not only a result of the synergistic effect of Pt and Ni but also because of the controlled size of the encapsulated Pt-Ni NPs in the dendrimers (see below).

3.3.3. Catalyst characterization

All the catalysts were characterized by UV–Vis spectroscopy. The UV–Vis spectra of G4-OH($Pt^{2+}_{x}Ni^{2+}_{60-x}$) before and after reduction as well as spectra of the starting materials (G4-OH, $NiCl_2$, K_2PtCl_4) are shown in Figures 3.5–3.7. The G4-OH PAMAM dendrimer exhibits a very weak absorption band at 285 nm, which corresponds to intraligand transitions. Fresh dendrimer/ Pt^{2+}-Ni^{2+} complexes with various Pt/Ni ratios exhibit a band at approximately 215 nm, which is a result of the presence of $PtCl_4^{2-}$ [17]. These bands disappear after stirring for 1 week (Figure 3.6), and another band appears at approximately 250 nm owing to the complexation of the metals with the dendrimer tertiary amines, which arises from ligand-to-metal charge transfer (LMCT). Notably, the intensities of the bands increase with increasing Pt content. After the reduction by $NaBH_4$, two significant spectral changes were observed (Figure 3.7). First, the intensity of the LMCT bands at 250 nm decrease, and second, there is an increased absorbance at longer wavelengths. These observations are consistent with the partial reduction of the Pt^{2+}/dendrimer complex by $NaBH_4$ [8, 17, 50]. However, Ni^{2+}/dendrimer complexes (G4-OH(Ni^{2+})$_{60}$) have a featureless absorbance (Figures 3.5 and 3.6), although they exhibit an increase in absorbance toward lower wavelengths after reduction (Figure 3.7), which is consistent with

previous spectroscopic observations for Ni DENs [51, 52].

To understand the states of Pt and Ni that coexist in the G4-OH($Pt_{12}Ni_{48}$) DENs, XPS with Ar sputtering was performed, which revealed that the Pt-Ni DENs were composed of Pt^0 and Ni^0 (Figure 3.8). After Ar sputtering, the Ni $2p_{3/2}$ and Ni $2p_{1/2}$ peaks for the G4-OH($Pt_{12}Ni_{48}$) DENs were observed with binding energies of 853.3 and 870.4 eV, respectively, which corresponds to metallic Ni^0 (Figure 3.8a) [53]. No shifts of these peaks were observed during Ar sputtering (240 min). However, the Pt $4f_{7/2}$ and Pt $4f_{5/2}$ peaks (73.5 and 76.7 eV, respectively), which correspond to Pt^{2+}, before Ar sputtering, shifted to 71.6 and 74.9 eV, respectively, which correspond to Pt^0, after Ar sputtering (4 min; Figure 3.8b) [53].

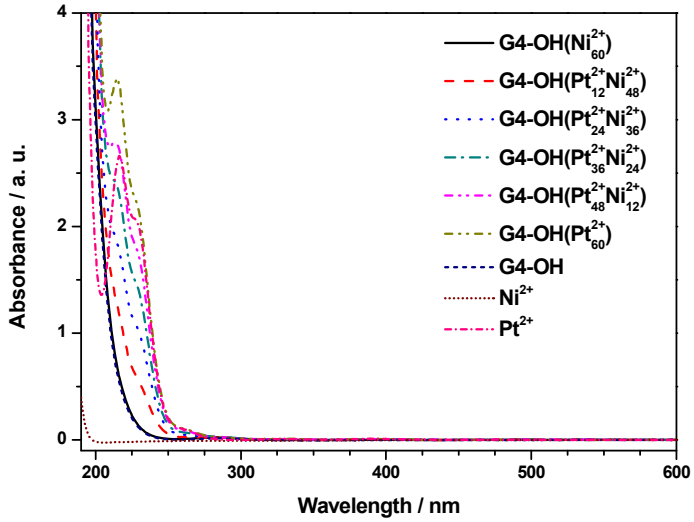

Figure 3.5. UV–Vis spectra of aqueous K_2PtCl_4, $NiCl_2$, G4-OH, and G4-OH($Pt^{2+}_xNi^{2+}_{60-x}$) (x = 0, 12, 24, 36, 48 and 60) freshly prepared. In all cases, the concentrations of total metal and G4-OH were 0.25 mM and 4.2 μM, respectively.

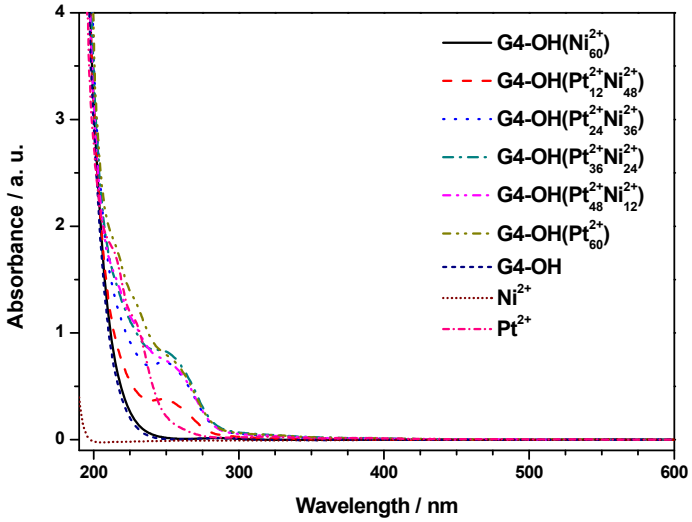

Figure 3.6. UV–Vis spectra of aqueous K_2PtCl_4, $NiCl_2$, G4-OH, and G4-OH($Pt^{2+}_{x}Ni^{2+}_{60-x}$) ($x$ = 0, 12, 24, 36, 48 and 60) after stirring for 1 week. In all cases, the concentrations of total metal and G4-OH were 0.25 mM and 4.2 μM, respectively.

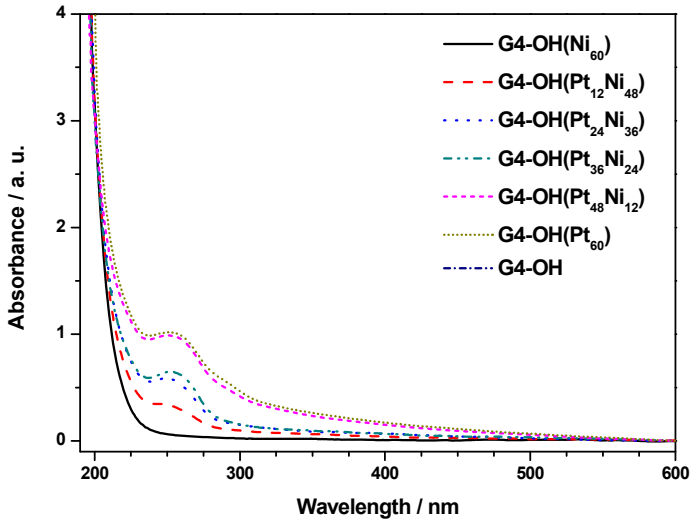

Figure 3.7. UV–Vis spectra of aqueous G4-OH(Pt_xNi_{60-x}) (x = 0, 12, 24, 36, 48 and 60) after reduction. In all cases, the concentrations of total metal and G4-OH were 0.25 mM and 4.2 μM, respectively.

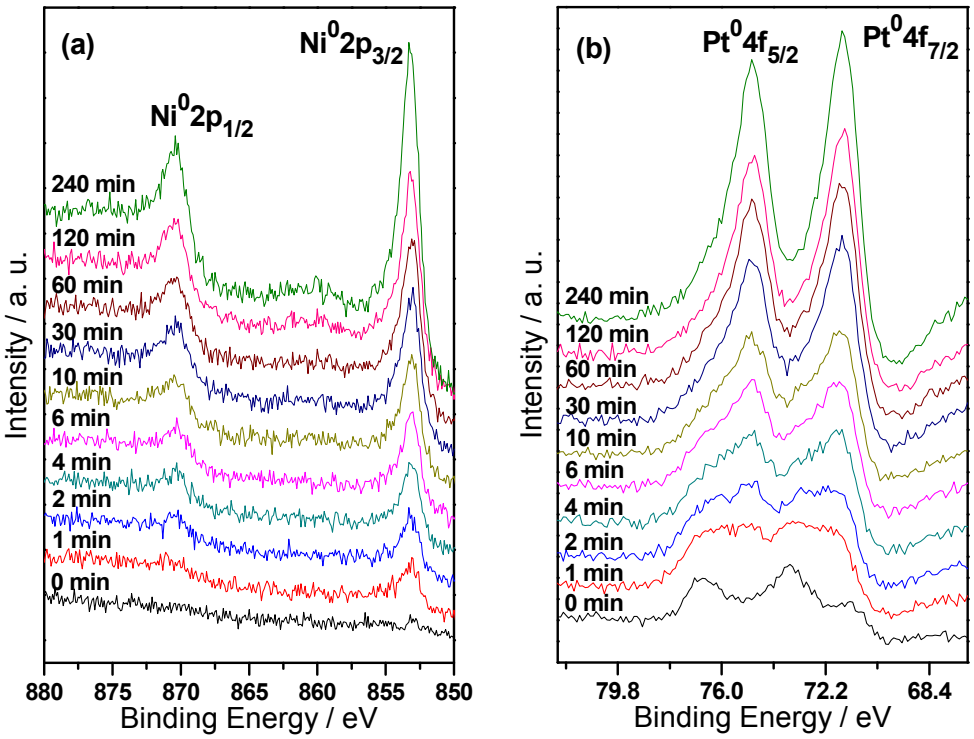

Figure 3.8. XPS spectra of (a) Ni and (b) Pt in the G4-OH($Pt_{12}Ni_{48}$) DENs before (0 min) and after (1 ~ 240 min) Ar sputtering.

These results suggest that the G4-OH($Pt_{12}Ni_{48}$) DENs contain both Pt^0 and Pt^{2+}, in which Pt^{2+} bonded to the amide N atoms of G4-OH PAMAM dendrimer and complexed Pt^{2+} cannot be reduced completely by $NaBH_4$ owing to the formation of a coordination sphere through a strong stabilizing chelate effect [8, 50]. No change in the Pt/Ni intensity ratio was observed after Ar sputtering (240 min), which indicates the homogeneity of the composition of the bimetallic Pt-Ni DENs.

To investigate the microstructure of the Pt-Ni DENs, TEM (HAADF-STEM and EDS) and SEM measurements were performed. The typical TEM, HAADF-STEM, and SEM images of the G4-OH($Pt_{12}Ni_{48}$) DENs (Figures 3.9–3.11) reveal that

size-controlled Pt-Ni NPs with an average particle size of 1.1 ± 0.3 nm are encapsulated in the G4-OH dendrimer. EDS analyses of points selected randomly and the bulk area (Figure 3.10) indicate uniform bimetallic Pt-Ni NPs. These results are in accord with the observation that the bimetallic Pt-Ni DENs show enhanced catalytic performance, whereas monometallic Pt DENs and Ni DENs show lower performances in the catalytic decomposition of hydrous hydrazine and hydrolysis of AB.

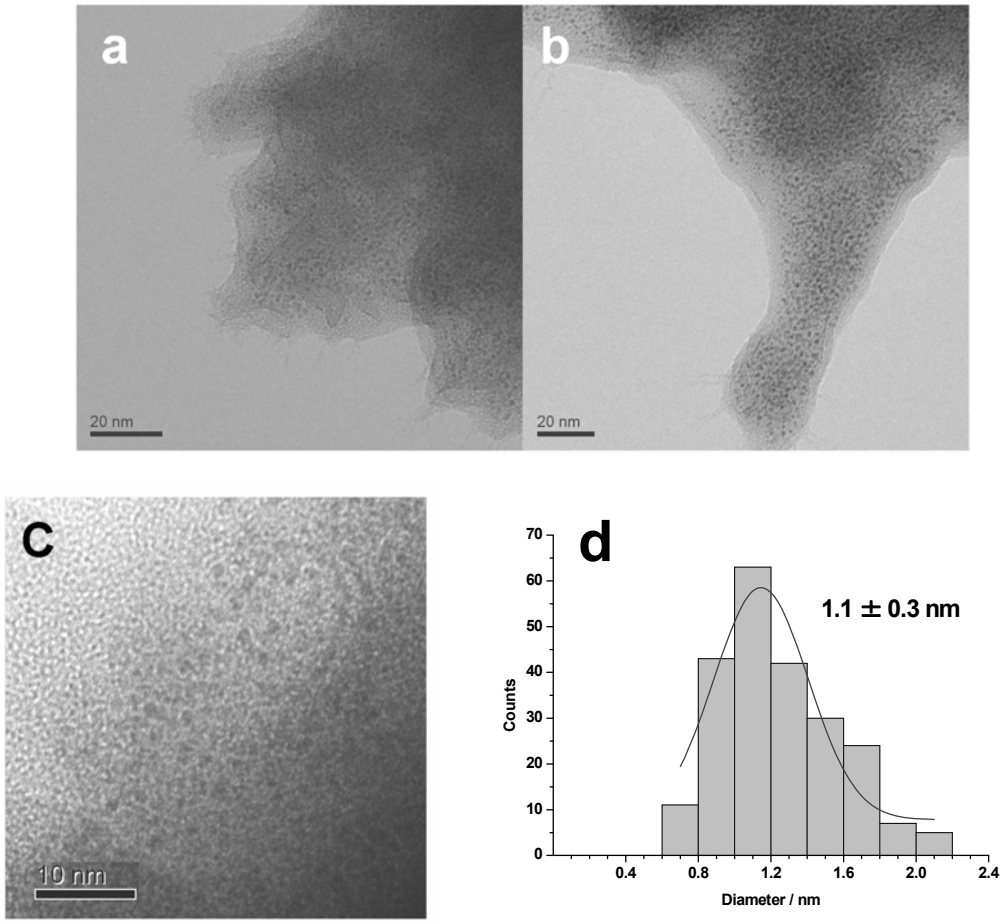

Figure 3.9. (a–c) TEM images and (d) the corresponding particle-size distribution of the G4-OH($Pt_{12}Ni_{48}$) DENs.

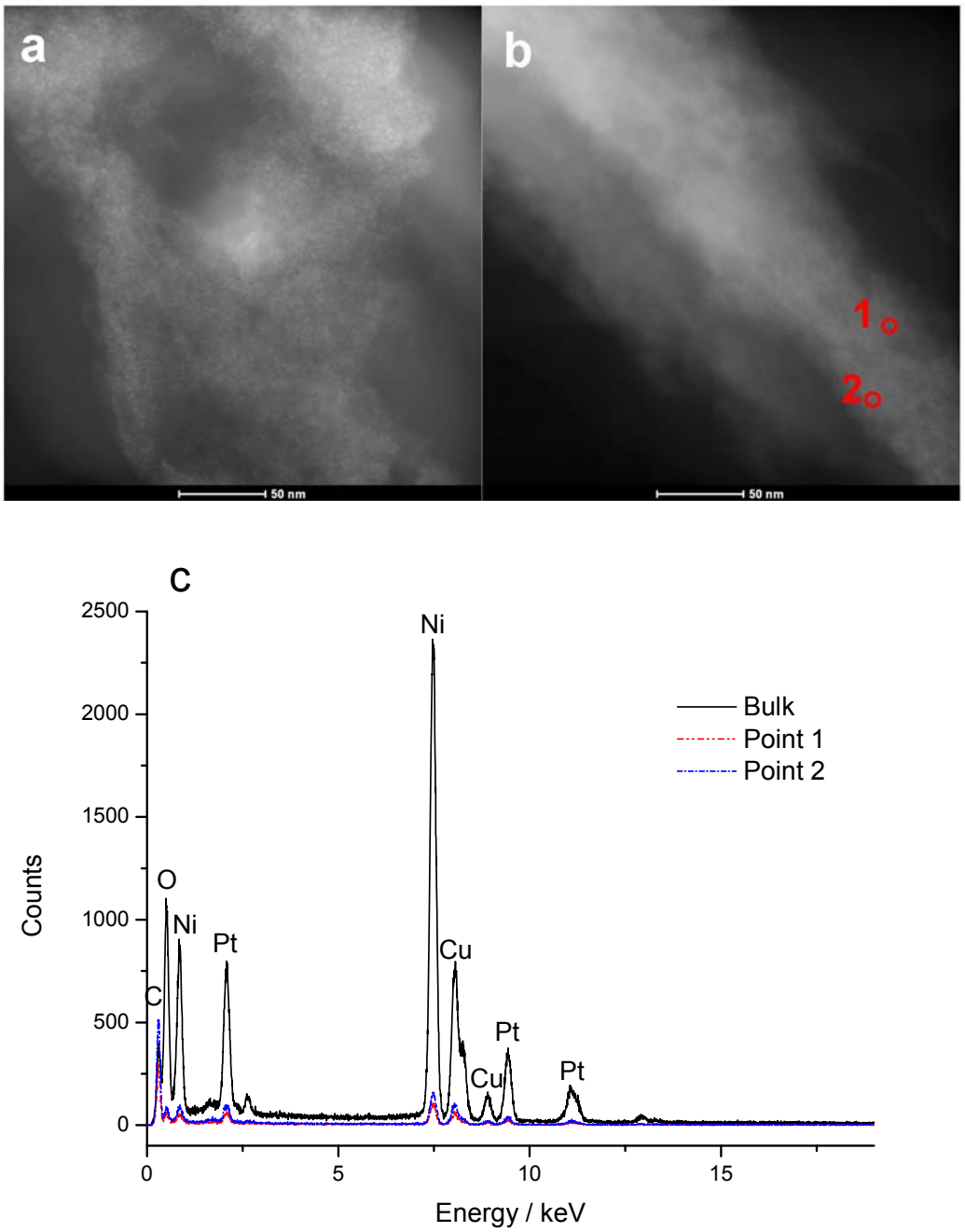

Figure 3.10. (a,b) HAADF-STEM images of G4-OH($Pt_{12}Ni_{48}$) DENs, and (c) the corresponding EDS spectra for the bulk area and points indicated in (b). Cu signals come from TEM grids.

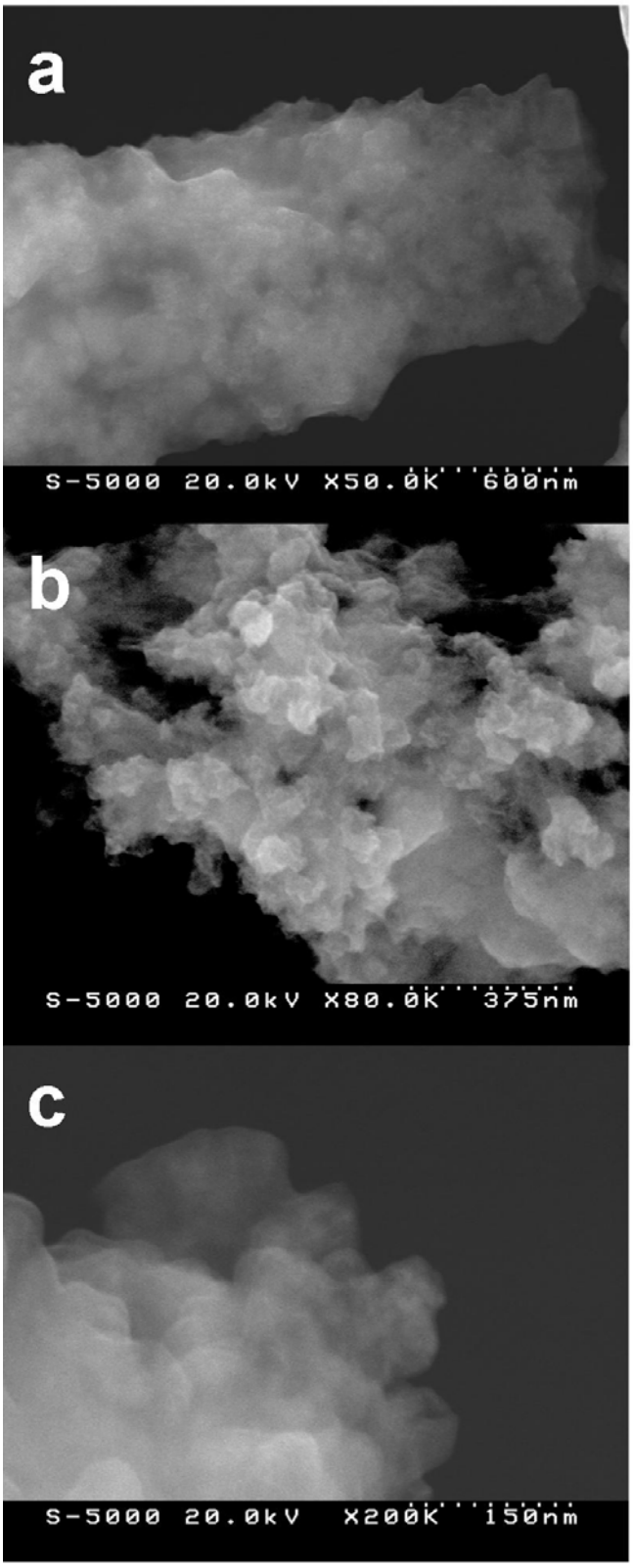

Figure 3.11. (a–c) SEM images of G4-OH($Pt_{12}Ni_{48}$) DENs.

3.4. Conclusion

We have demonstrated that highly dispersed bimetallic Pt-Ni nanoparticles encapsulated in G4-OH PAMAM dendrimers exhibit excellent performances as catalysts for the selective decomposition of hydrous hydrazine and the hydrolysis of AB. The synergistic effect of Ni and Pt coupled with the dendrimer-controlled small size of the nanoparticles account for the excellent catalytic performance. Although monometallic Ni DENs have a very low activity and hydrogen selectivity and Pt DENs are inactive for the decomposition of hydrous hydrazine, bimetallic G4-OH($Pt_{12}Ni_{48}$) DENs efficiently catalyze the decomposition of hydrous hydrazine to hydrogen and nitrogen with 100% selectivity at 343 K in the presence of NaOH (0.4 M). Additionally, bimetallic Pt-Ni DENs show excellent catalytic performance for the hydrolysis of AB at room temperature. The bimetallic Pt-Ni DENs present a step toward a high-performance catalyst system that will open the door to exploit hydrous hydrazine and AB as promising, practical materials for hydrogen storage.

References

[1] R. M. Crooks, M. Zhao, L. Sun, V. Chechik, L. K. Yeung, *Acc. Chem. Res.* **2001**, *34*, 181–190.

[2] R. W. J. Scott, H. Ye, R. R. Henriquez, R. M. Crooks, *Chem. Mater.* **2003**, *15*, 3873–3878.

[3] P. K. Maiti, T. Çağin, G. Wang, W. A. Goddard III, *Macromolecules* **2004**, *37*, 6236–6254.

[4] T. Mizugaki, M. Murata, S. Fukubayashi, T. Mitsudome, K. Jitsukawa, K. Kaneda,

Chem. Commun. **2008**, 241–243.

[5] Y. Niu, L. K. Yeung, R. M. Crooks, *J. Am. Chem. Soc.* **2001**, *123*, 6840–6846.

[6] R. W. J. Scott, O. M. Wilson, R. M. Crooks, *J. Phys. Chem. B* **2005**, *109*, 692–704.

[7] K. Yamamoto, T. Imaoka, W. J. Chun, O. Enoki, H. Katoh, M. Takenaga, A. Sonoi, *Nat. Chem*. **2009**, *1*, 397–402.

[8] Y. Borodko, C. M. Thompson, W. Huang, H. B. Yildiz, H. Frei, G. A. Somorjai, *J. Phys. Chem. C* **2011**, *115*, 4757–4767.

[9] R. W. J. Scott, A. K. Datye, R. M. Crooks, *J. Am. Chem. Soc.* **2003**, *125*, 3708–3709.

[10] Y. M. Chung, H. K. Rhee, *Catal. Surv. Asia* **2004**, *8*, 211–223.

[11] J. C. Garcia-Martinez, R. Lezutekong, R. M. Crooks, *J. Am. Chem. Soc*. **2005**, *127*, 5097–5103.

[12] X. Peng, Q. Pan, G. L. Rempel, S. Wu, *Catal. Comm*. **2009**, *11*, 62–66.

[13] I. Nakamula, Y. Yamanoi, T. Imaoka, K. Yamamoto, H. Nishihara, *Angew. Chem. Int. Ed.* **2011**, *50*, 5830–5833.

[14] S. N. S. Goubert-Renaudin, A. Wieckowski, *J. Electroanal. Chem*. **2011**, *652*, 44–51.

[15] Y. G. Kim, S. K. Oh, R. M. Crooks, *Chem. Mater.* **2004**, *16*, 167–172.

[16] H. Ye, R. M. Crooks, *J. Am. Chem. Soc*. **2007**, *129*, 3627–3633.

[17] M. R. Knecht, M. G. Weir, V. S. Myers, W. D. Pyrz, H. Ye, V. Petkov, D. J. Buttrey, A. I. Frenkel, R. M. Crooks, *Chem. Mater*. **2008**, *20*, 5218–5228.

[18] H. L. Jiang, S. K. Singh, J. M. Yan, X. B. Zhang, Q. Xu, *ChemSusChem* **2010**, *3*, 541–549.

[19] M. Yadav, Q. Xu, *Energy Environ. Sci*. **2012**, *5*, 9698–9725.

[20] T. F. Hung, H. C. Kuo, C. W. Tsai, H. M. Chen, R. S. Liu, B. J. Weng, J. F. Lee, *J. Mater. Chem*. **2011**, *21*, 11754–11759.

[21] U. B. Demirci, P. Miele, *Energy Environ. Sci*. **2011**, *4*, 3334–3341.

[22] Z. Huang, T. Autrey, *Energy Environ. Sci*. **2012**, *5*, 9257–9268.

[23] S. K. Singh, X. B. Zhang, Q. Xu, *J. Am. Chem. Soc*. **2009**, *131*, 9894–9895.

[24] S. K. Singh, Q. Xu, *J. Am. Chem. Soc*. **2009**, *131*, 18032–18033.

[25] S. K. Singh, Q. Xu, *Inorg. Chem*. **2010**, *49*, 6148–6152.

[26] S. K. Singh, Q. Xu, *Chem. Commun*. **2010**, *46*, 6545–6547.

[27] S. K. Singh, Z. H. Lu, Q. Xu, Eur. *J. Inorg. Chem*. **2011**, 2232–2237.

[28] S. K. Singh, Y. Iizuka, Q. Xu, Int. *J. Hydrogen Energy* **2011**, *36*, 11794–11801.

[29] S. K. Singh, A. K. Singh, K. Aranishi, Q. Xu, *J. Am. Chem. Soc*. **2011**, *133*, 19638–19641.

[30] A. K. Singh, M. Yadav, K. Aranishi, Q. Xu, *Int. J. Hydrogen Energy* **2012**, *37*, 18915–18919.

[31] L. He, Y. Huang, A. Wang, X. Wang, X. Chen, J. J. Delgado, T. Zhang, *Angew. Chem. Int. Ed*. **2012**, *51*, 6191–6194.

[32] T. He, H. Wu, G. Wu, J. Wang, W. Zhou, Z. Xiong, J. Chen, T. Zhang, P. Chen, *Energy Environ. Sci*. **2012**, *5*, 5686–5689.

[33] N. Hazari, *Chem. Soc. Rev*. **2010**, *39*, 4044–4056.

[34] J. M. Chin, R. R. Schrock, P. Müller, *Inorg. Chem*. **2010**, *49*, 7904–7916.

[35] T. Murakami, T. Nishikiori, T. Nohira, Y. Ito, *J. Am. Chem. Soc*. **2003**, *125*, 334–335.

[36] V. Smil, *Enriching the Earth: Fritz Haber, Carl Bosch, and the Transformation of World Food Production*, MIT Press, Cambridge, **2004**.

[37] S. Sridhar, T. Srinivasan, U. Virendra, A. A. Khan, Membrane Separations and Process Development Group, *Chem. Eng. J*. **2003**, *94*, 51–56.

[38] H. Hayashi, Res. *Chem. Intermed*. **1998**, *24*, 183–196.

[39] H. Hayashi, *Catal. Rev*. **1990**, *32*, 229–277.

[40] A. Gutowska, L. Li, Y. Shin, C. M. Wang, X. S. Li, J. C. Linehan, R. S. Smith, B. D. Kay, B. Schmid, W. Shaw, M. Gutowski, T. Autrey, *Angew. Chem. Int. Ed*. **2005**, *44*, 3578–3582.

[41] M. Chandra, Q. Xu, *J. Power Sources* **2006**, *156*, 190–194.

[42] Q. Xu, M. Chandra, *J. Power Sources* **2006**, *163*, 364–370.

[43] P. Z. Li, A. Aijaz, Q. Xu, *Angew. Chem. Int. Ed*. **2012**, *51*, 6753–6756.

[44] C. W. Hamilton, R. T. Baker, A. Staubitz, I. Manners, *Chem. Soc. Rev*. **2009**, *38*, 279–293.

[45] S. K. Kim, W. S. Han, T. J. Kim, T. Y. Kim, S. W. Nam, M. Mitoraj, Ł. Piekoś, A. Michalak, S. J. Hwang, S. O. Kang, *J. Am. Chem. Soc*. **2010**, *132*, 9954–9955.

[46] C. Y. Cao, C. Q. Chen, W. Li, W. G. Song, W. Cai, *ChemSusChem* **2010**, *3*, 1241–1244.

[47] H. L. Jiang, Q. Xu, *J. Mater. Chem*. **2011**, *21*, 13705–13725.

[48] F. Cheng, H. Ma, Y. Li, J. Chen, *Inorg. Chem*. **2007**, *46*, 788–794.

[49] X. Yang, F. Cheng, J. Liang, Z. Tao, J. Chen, *Int. J. Hydrogen Energy* **2009**, *34*, 8785–8791.

[50] W. Huang, J. N. Kuhn, C. K. Tsung, Y. Zhang, S. E. Habas, P. Yang, G. A. Somorjai, *Nano Lett*. **2008**, *8*, 2027–2034.

[51] K. A. Marvin, N. N. Thadani, C. A. Atkinson, E. L. Keller, K. J. Stevenson, *Chem. Commun*. **2012**, *48*, 6289–6291.

[52] M. R. Knecht, J. C. Garcia-Martinez, R. M. Crooks, *Chem. Mater*. **2006**, *18*, 5039–5044.

[53] C. D. Wagner, W. N. Riggs, L. E. Davis, J. F. Moulder, *Handbook of X-Ray Photoelectron Spectroscopy: A Reference Book of Standard Spectra for Use In X-Ray Photoelectron Spectroscopy* (Ed.: G. E. Muilenberg), Physical Electronics Division Perkin–Elmer Corp., Minnesota, **1978**.

Chapter 4

Dendrimer-encapsulated Co nanoparticles as high-performance catalyst for hydrolysis of ammonia borane

4.1. Introduction

Dendrimers are very exiting cascade type three-dimensional polymers that have well-defined molecular weight/size, uniform dense terminal/internal functional groups, and porosity, and are found to be very important for encapsulation of metal salts and formation of nanoparticles (NPs)/-clusters of desired sizes according to the sites present in them. Generally, dendrimers of low generation tend to exist in relatively open forms, at higher generations ($G \geq 4.0$) take intrinsically well-defined globular structure [1–3]. A poly(amidoamine) (PAMAM) dendrimer is highly branched macromolecule containing interior tertiary amine groups which can effectively coordinate with metal ions. Such metal ions may then be reduced to form encapsulated metal particles that can be highly stable in solution. Since the same number of chelating sites is present in all dendrimer molecules, this process can yield mono-disperse metal nanoparticles [4–6].

Recently, hydroxyl-terminated PAMAM dendrimers have been used as templates for the synthesis of mono- and bimetallic dendrimer-encapsulated NPs (DENs) in the ~1–2 nm size range and as a macro ligand for stabilizing metallic NPs [7–9]. The synthesis of DENs is generally carried out in two steps. First, a metal salt is introduced into a dendrimer-containing solution, and the resulting cations form the complexation at the dendrimer interior amines. Second, the encapsulated metal ions are chemically

reduced using an appropriate reducing agent, such as $NaBH_4$, which results in the formation of zero valent DENs. The applications of DENs in catalytic reactions also have been intensively studied and they offered promising new opportunities to create tailored catalytic systems [9–14].

On the other hand, the world's energy consumption is dramatically increasing owing to the rising standards of living and the growing population. This increasing energy demand will require enormous growth in the energy generation capacity, more secure and diversified energy sources, and a successful strategy to decrease greenhouse gas emissions. Among the various alternative energy strategies, hydrogen, a globally accepted clean fuel and a primary carrier that connects plenty of energy sources to different end uses, such as hydrogen fuel cell vehicles and portable electronics, will enable a secure and clean energy future [15]. Among the potential candidates for effective chemical hydrogen storage, ammonia borane (AB, NH_3BH_3) has a hydrogen content of 19.6 wt%, which exceeds that of gasoline, and is accordingly an attractive candidate for chemical hydrogen-storage applications [16–34]. There are significant reports of hydrogen generation from AB by thermal decomposition [16, 17] and catalytic hydrolysis under milder conditions [18–34]. However, it is still big challenge to develop efficient, economical, and durable catalysts to further improve the kinetic properties under moderate reaction conditions. The catalytic hydrolysis of AB reaction can be briefly expressed as follows (Equation 4.1).

$$NH_3BH_3 + 2H_2O \longrightarrow NH_4^+ + BO_2^- + 3H_2 \qquad (4.1)$$

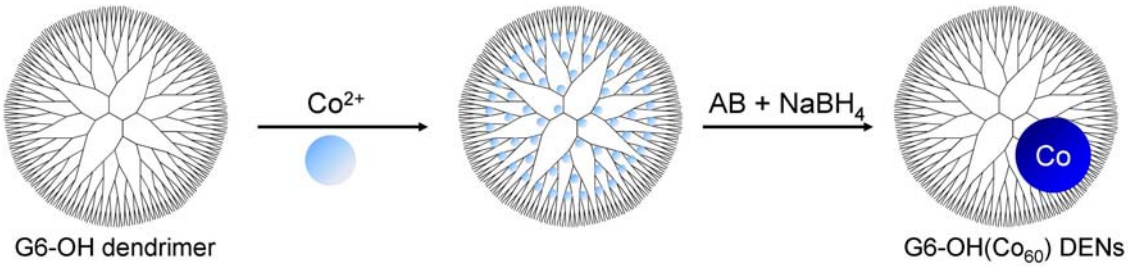

Scheme 3.1. Schematic representation of the synthesis of dendrimer-encapsulated Co nanoparticles.

In this work, we have prepared Co DENs by the complexation of Co^{2+} cations to the internal tertiary amine of sixth-generation hydroxyl-terminated PAMAM dendrimers (G6-OH) followed by reduction by AB and $NaBH_4$ (Scheme 4.1) and investigated the catalytic performance for hydrogen generation from the hydrolysis of AB.

4.2. Experimental Section

4.2.1. Chemicals

Commercial chemicals were used as received for catalyst preparation and catalytic reactions. Ammonia borane (AB, 97%) was purchased from JSC Aviabor. $NaBH_4$ (98.5%), and sixth-generation hydroxyl-terminated PAMAM dendrimers (G6-OH, 5 wt% in methanol, Mw = 58304) were purchased from Sigma–Aldrich. $CoCl_2 \cdot 6H_2O$ (99.0%) was purchased from Wako Pure Chemical Industries. Deionized H_2O with a specific resistance of 17.5 MΩ cm was obtained by reversed osmosis followed by ion-exchange and filtration (RFD250NB, Toyo Roshi Kaisha, Ltd., Japan).

4.2.2. Syntheses of dendrimer-encapsulated Co nanoparticles

Co DENs were prepared according to a procedure reported by Crooks and co-workers [10]. Briefly, an aqueous solution of $CoCl_2 \cdot 6H_2O$ (10 mM, 1 mL) was added to an aqueous solution of G6-OH, which was prepared in advance by drying to remove methanol from the solution. The dendrimer-to-metal molar ratio was adjusted to 1:60. The metal complex and dendrimer solution was stirred for over night in a 30-mL two-necked round-bottom flask to allow the Co^{2+} cations to fully complex with the interior amines of the dendrimers. $NaBH_4$ (4 mg) and ammonia borane (0.8 M, 1 mL) were added to the solution with vigorous shaking, which caused the color of the solution to change from colourless to black. The resulting G6-OH(Co_{60}) DENs were characterized and used for the catalytic reactions.

4.2.3. Catalytic reaction of AB hydrolysis

The catalytic hydrolysis of AB was performed following our procedure reported previously [20–29]. Typically, an aqueous solution of AB (0.8 M, 1 mL) was injected to a glass reactor that contained an aqueous suspension of Co DENs to initiate the hydrolysis of AB. The catalyst/AB ratio was fixed at 0.013. The reactions were carried out at different temperatures (298, 303, 308, 313, 318, and 323 K) by using a water bath. The gas released during the reaction was passed through a HCl solution (1.0 M) before it was measured volumetrically. The prepared Co DENs were used for durability tests. A new catalytic run was started by adding an additional equivalent amount of aqueous AB solution (0.8 M, 1 mL) and the evolution of gas was monitored as described above. Mass spectra of the generated gases were collected by using a Balzers Prisma QMS 200 mass spectrometer.

4.2.4. Catalyst characterization

Ultraviolet-visible (UV–Vis) absorption spectra were recorded by using a Shimadzu UV-2550 spectrophotometer in the wavelength range of 190–800 nm and corrected using aqueous solution as background. X-ray photoelectron spectroscopy (XPS) analysis was carried out on a Shimadzu ESCA-3400 X-ray photoelectron spectrometer using an Mg K source (10 kV, 10 mA). The Ar sputtering experiments were carried out under the conditions of background vacuum 3.4 x 10^{-6} Pa, sputtering acceleration voltage of 2 kV and sputtering current of 10 mA. Transmission electron microscope (TEM, FEI TECNAI G2), and energy-dispersive X-ray spectroscopy (EDS) were used to determine the detailed microstructure of Co DENs. The TEM (EDS) samples were prepared by depositing one or two droplets of the NPs suspended in a solution onto amorphous carbon-coated Cu grids, which were then dried under Ar atmosphere.

4.3. Results and discussion

4.3.1. Characterization of Co DENs

G6-OH PAMAM dendrimer is approximately 6.7 nm in diameter and contain 254 interior tertiary amine groups and 256 surface functional groups. An aqueous solution of Co precursor, $CoCl_2$, was added to the as-prepared G6-OH aqueous solution and the dendrimer-to-metal molar ratio was adjusted to 1:60. After vigorous shaking for over night to allow the Co^{2+} cations to fully complex with the interior tertiary amines of the dendrimers (G6-OH$(Co^{2+})_{60}$), excess $NaBH_4$ and AB were used to reduce Co^{2+} cations and finally the Co DENs (G6-OH(Co_{60})) were obtained. Co DENs were characterized by UV–Vis spectroscopy. The UV–Vis spectra of G6-OH$(Co^{2+})_{60}$ before and after reduction as well as the spectrum of the starting materials (G6-OH, $CoCl_2$) are shown in Figure 4.1. The G6-OH PAMAM dendrimer exhibits a weak absorption band at 285 nm,

which corresponds to intraligand transitions, and $CoCl_2$ exhibits a broad band at approximately 510 nm, which is a result of the presence of Co^{2+} in the solution. On the other hand, two characteristic spectral features were observed for G6-OH$(Co^{2+})_{60}$. First, the intensity of the band at 285 nm decreases, and second, there is no absorbance at 510 nm. These observations indicate that the Co^{2+} cations were bound to the tertiary inner nitrogen atoms. After the reduction by $NaBH_4$ and AB, there is an increased absorbance in a wide range of long wavelengths. These results indicate the forming of Co NPs and are consistent with previous spectroscopic observations for other DENs [35, 36].

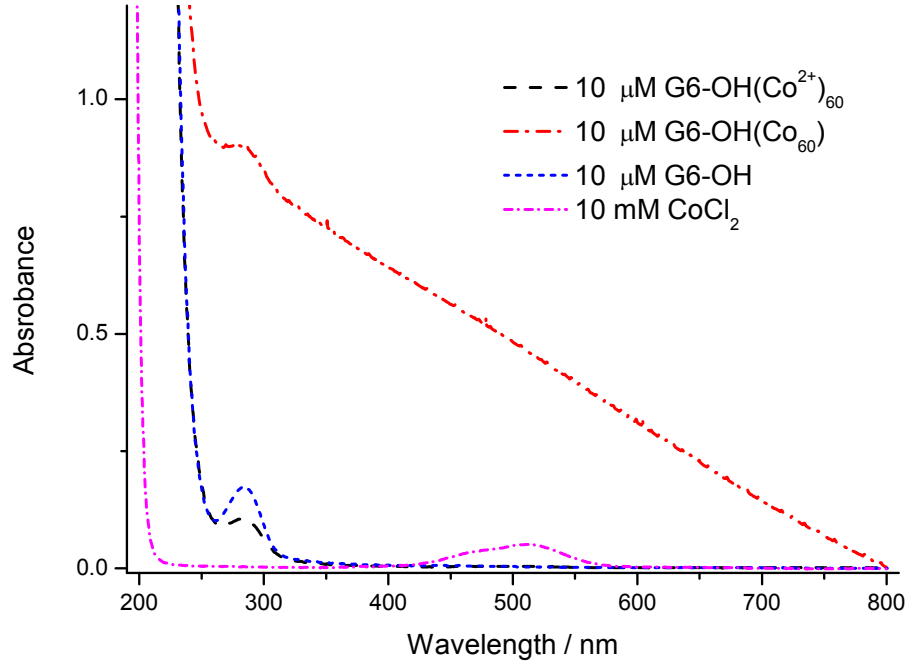

Figure 4.1. UV–Vis spectra of aqueous solutions containing G6-OH$(Co^{2+})_{60}$, G6-OH(Co_{60}), G6-OH, and $CoCl_2$. The concentrations of G6-OH$(Co^{2+})_{60}$, G6-OH(Co_{60}), and G6-OH were 10 μM, respectively. The spectrum of $CoCl_2$ (10 mM) was shown as reference.

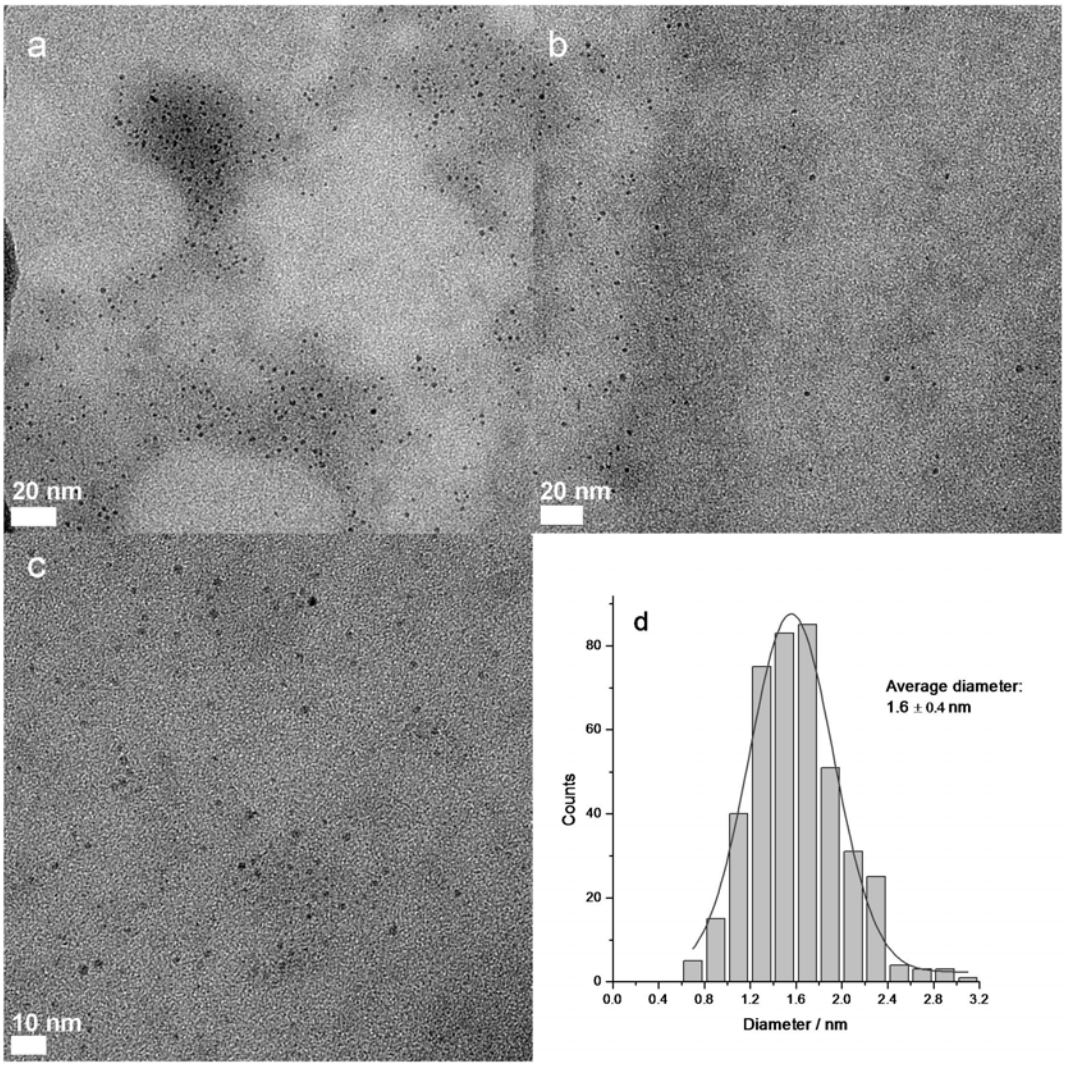

Figure 4.2. (a-c) TEM images with different magnifications and (d) the corresponding particle-size distribution histogram of G6-OH(Co_{60}) DENs. The average diameter of Co DENs is 1.6 ± 0.4 nm.

To investigate the morphology of the Co DENs, TEM were used. TEM observations revealed that the resultant G6-OH(Co_{60}) DENs are very fine and highly monodispersed. The average particle size of 1.6 ± 0.4 nm (Figure 4.2d) is slightly larger than the calculated value for a 60-atom fcc packed Co cluster (1.1 nm) [37]. Note that only the Co NPs have sufficient contrast to appear in these images; the dendrimer itself is

transparent. EDS analysis of randomly selected areas (Figure 4.3) also indicate that a uniform monometallic Co DENs were formed.

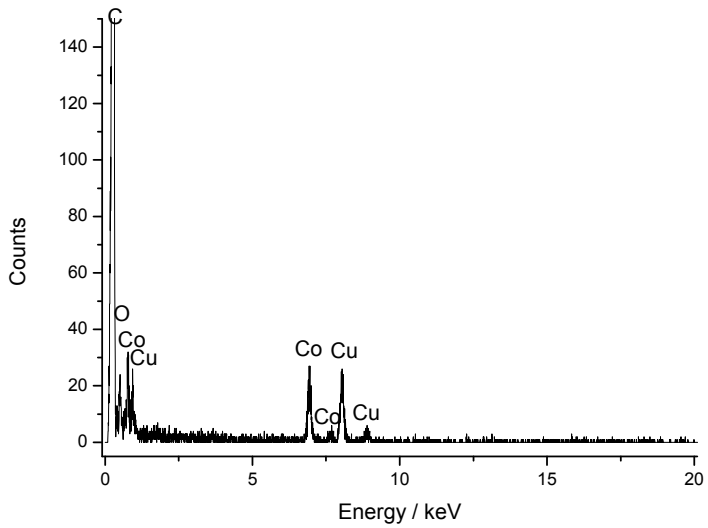

Figure 4.3. EDS spectrum for the area corresponding to Figure 4.2c. Cu signals come from TEM grids.

To understand Co oxidation state in the G6-OH(Co_{60}) DENs, XPS measurements with Ar sputtering were carried out (Figure 4.4). Before Ar sputtering, broad Co $2p_{3/2}$ and Co $2p_{1/2}$ peaks for G6-OH(Co_{60}) DENs were observed with binding energies of 782.6 and 798.1 eV, respectively, which correspond to the Co^{2+} state [38]. The observed peaks for Co^{2+} are due to CoO, which are caused by oxygen in the Air during the sample preparation. Note that even if the NPs are noble metal, sub-nanometer sizes of metallic particles tend to be oxidized easily. These peaks were shifted to 778.4 and 793.5 eV, corresponding to Co^0, after Ar sputtering (10 min) [38]. These results suggest that Co^{2+} bound to tertiary amide nitrogen atoms of G6-OH PAMAM dendrimer were completely reduced by $NaBH_4$ and AB, forming G6-OH(Co_{60}) DENs.

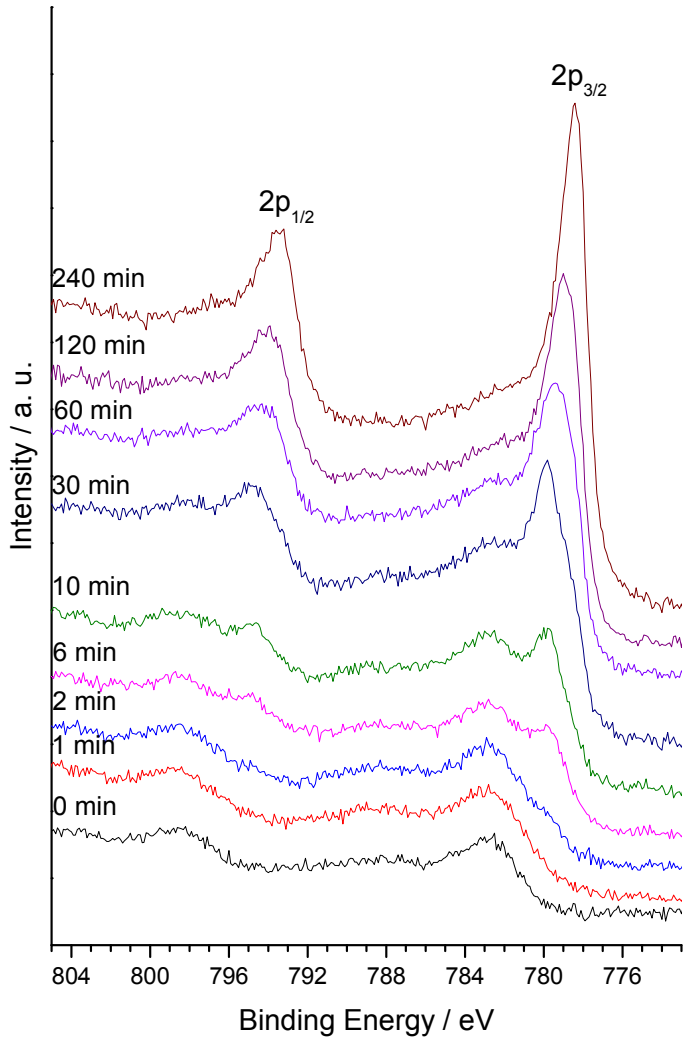

Figure 4.4. XPS spectra of Co in the G6-OH(Co_{60}) DENs before (0 min) and after (1–240 min) Ar sputtering.

4.3.2. Catalytic hydrolysis of ammonia borane

The as-synthesized G6-OH$(Co)_{60}$ DENs have been applied as catalysts for hydrolysis of AB. Reaction was initiated by introducing aqueous AB solution into the reaction flask containing the as-synthesized G6-OH$(Co)_{60}$ catalyst with vigorous shaking at room as well as elevated temperatures. H_2 generated from the AB hydrolysis

was collected in the buret, with which the H_2 volume was monitored. Figure 4.5 shows the profiles of hydrogen generation from aqueous AB solution (0.8 M, 1.0 mL) *vs*. reaction time catalyzed by G6-OH$(Co)_{60}$ DENs at different reaction temperatures controlled by a water bath. Catalyst G6-OH$(Co)_{60}$ DENs catalyzed hydrolysis of AB at room temperature with the release of 3.0 equivalents of hydrogen (Figure 4.5, 298 K), which indicates complete hydrogen generation from AB according to Equation 4.1. The evolution of H_2 was confirmed by mass spectrometry. The catalytic AB hydrolysis reaction was completed in 30 min at room temperature (298 K), corresponding to a turnover frequency (TOF) value of 7.7 mol_{H_2} mol_{metal}^{-1} min^{-1} (Figures 4.5 and 4.6). The TOF value at room temperature is quite high in comparison to the supported Co catalysts reported for hydrolysis of AB [21, 24, 26]. According to the previous works [22, 23, 25], non-noble metal NPs, such as Fe, Ni and Co, prepared by using a mixture of AB and $NaBH_4$ as reducing agents show higher catalytic activities for hydrolysis of AB. Also, it is well-known that the catalytic activity generally increases with the decrease of metal nanoparticle size, as smaller metal nanoparticles have higher surface areas available for reactants. Accordingly, the fine size and monodisperse nature of Co DENs (1.6 ± 0.4 nm) are responsible to such a high catalytic activity and high superiority than previously reported Co NPs supported on γ-Al_2O_3, SiO_2 and carbon [21, 24, 26]. In addition, these completely confined ultrafine metal nanoparticles within PAMAM dendrimers could be used as catalyst for different catalytic reactions.

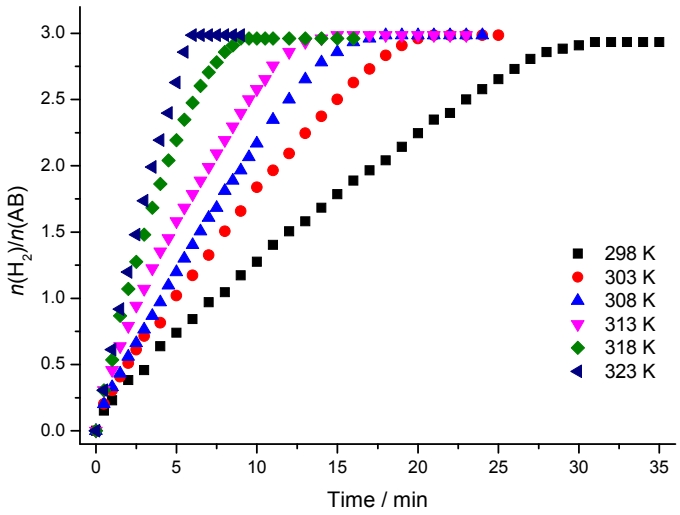

Figure 4.5. Temperature effects on hydrogen generation rate catalyzed by G6-OH(Co_{60}) DENs from AB hydrolysis (0.8 M, 1.0 mL, Catalyst/AB = 0.013) at different reaction temperatures.

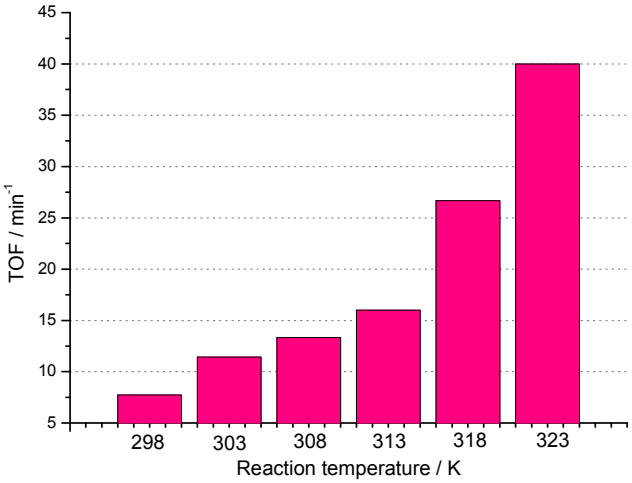

Figure 4.6. TOF values of hydrogen generation from AB hydrolysis catalyzed by G6-OH(Co_{60}) DENs (0.8 M, 1.0 mL, Catalyst/AB = 0.013) at different reaction temperatures.

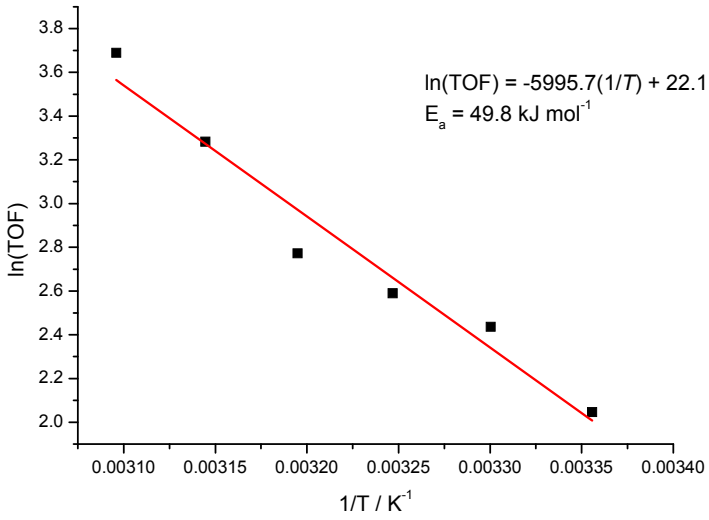

Figure 4.7. Arrhenius plot (ln(TOF) *vs.* 1/*T*) obtained from the data of Figure 4.6.

In addition, the hydrogen evolution rate from the hydrolysis of AB greatly depends on the reaction temperature. Figure 4.5 shows that the catalytic AB hydrolysis reactions were completed in 30, 20, 18, 13, 9 and 6 min at 298, 303, 308, 313, 318 and 323 K, respectively, which correspond to TOF values of 7.7, 11.4, 13.3, 16.0, 26.7 and 40.0 mol_{H_2} mol_{metal}^{-1} min^{-1} (Figures 4.5 and 4.6). Co DENs showed the highest catalytic performance at 323 K; reasonably as temperature increases TOF value enhances proportionally. Figure 4.7 shows the values calculated from the TOF values of hydrolysis of AB at different reaction temperatures in ln(TOF) *vs*. (1/T) axes. The Arrhenius plot was shown in Figure 4.7, which provides an activation energy (E_a) of 49.8 kJ mol^{-1}.

Catalyst durability is very important for practical applications. In most cases, the NPs get aggregated during the reaction and make the kinetics very slow. Therefore functionalized dendrimers could be a good choice for improving catalytic activities and durabilities. Interestingly, it is found that the productivity of H_2 over the G6-OH$(Co)_{60}$

catalyst almost remained unchanged after four runs, indicating the high durability in AB hydrolysis (Figure 4.8).

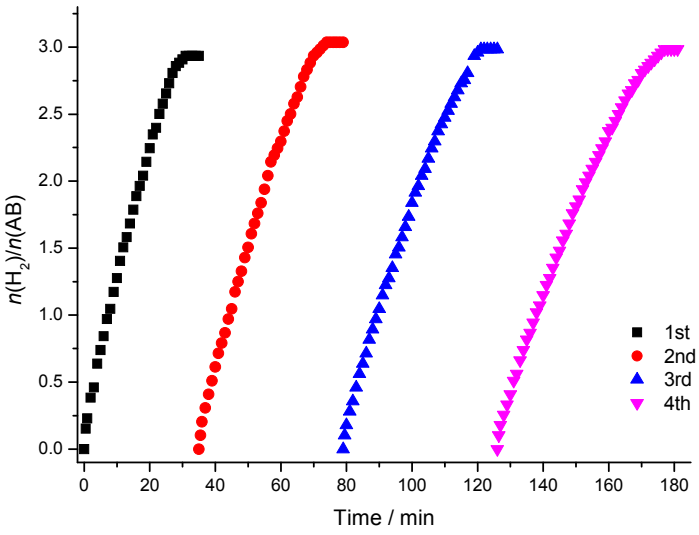

Figure 4.8. Hydrogen generation from aqueous AB solution catalyzed by G6-OH(Co_{60}) DENs at room temperature (0.8 M, 1.0 mL, Catalyst/AB = 0.013) in the 1st, 2nd, 3rd, and 4th runs carried out by addition of equivalent amounts of AB.

4.4. Conclusion

In summary, we have successfully synthesized dendrimer-encapsulated Co nanoparticles via complexation of Co^{2+} cations to internal tertiary amines of PAMAM dendrimer and reduction process by AB and $NaBH_4$. The synthesized Co DENs are highly dispersed with very narrow size distribution (1.6 ± 0.4 nm). Co DENs exhibit an excellent performance as catalyst for hydrolysis of AB at room temperature with significant high TOF value and good durability. The hydrolysis of AB at different reaction temperatures also reveals the activation energy of 49.8 kJ mol^{-1} on Co DENs.

Co DENs present a step toward a high-performance catalyst system, which will open a door to exploiting ammonia borane as a highly promising practical material for hydrogen storage.

References

[1] D. A. Tomalia, A. M. Naylor, W. A. Goddard III, *Angew. Chem. Int. Ed.* **1990**, *29*, 138–175.

[2] J. F. G. A. Jansen, E. M. M. de Brabander-van den Berg, E. W. Meijer, *Science* **1994**, *266*, 1226–1229.

[3] J. F. G. A. Jansen, E. W. Meijer, *J. Am. Chem. Soc.* **1995**, *117*, 4417–4418.

[4] M. Zhao, L. Sun, R. M. Crooks, *J. Am. Chem. Soc.* **1998**, *120*, 4877–4878.

[5] K. Esumi, A. Suzuki, N. Aihara, K. Usui, K. Torigoe, *Langmuir* **1998**, *14*, 3157–3159.

[6] S. H. Medina, M. E. H. El-Sayed, *Chem. Rev.* **2009**, *109*, 3141–3157.

[7] Y. M. Chung, H. K. Rhee, *Catal. Surv. Asia* **2004**, *8*, 211–223.

[8] Y. Borodko, C. M. Thompson, W. Huang, H. B. Yildiz, H. Frei, G. A. Somorjai, *J. Phys. Chem. C* **2011**, *115*, 4757–4767.

[9] K. Aranishi, A. K. Singh, Q. Xu, *ChemCatChem* **2013**, *5*, 2248–2252.

[10] R. M. Crooks, M. Zhao, L. Sun, V. Chechik, L. K. Yeung, *Acc. Chem. Res.* **2001**, *34*, 181–190.

[11] R. W. J. Scott, O. M. Wilson, R. M. Crooks, *J. Phys. Chem. B* **2005**, *109*, 692–704.

[12] T. Mizugaki, M. Murata, S. Fukubayashi, T. Mitsudome, K. Jitsukawa, K. Kaneda, *Chem. Commun.* **2008**, 241–243.

[13] K. Yamamoto, T. Imaoka, W. J. Chun, O. Enoki, H. Katoh, M. Takenaga, A. Sonoi, *Nat. Chem.* **2009**, *1*, 397–402.

[14] I. Nakamula, Y. Yamanoi, T. Imaoka, K. Yamamoto, H. Nishihara, *Angew. Chem. Int. Ed.* **2011**, *50*, 5830–5833.

[15] *Hydrogen as a Future Energy Carrier* (Eds.: A. Züttel, A. Borgschulte, L. Schlapbach), Wiley-VCH, Weinheim, **2008**.

[16] A. Gutowska, L. Li, Y. Shin, C. M. Wang, X. S. Li, J. C. Linehan, R. S. Smith, B. D. Kay, B. Schmid, W. Shaw, M. Gutowski, T. Autrey, *Angew. Chem. Int. Ed.* **2005**, *44*, 3578–3582.

[17] C. W. Hamilton, R. T. Baker, A. Staubitz, I. Manners, *Chem. Soc. Rev.* **2009**, *38*, 279–293.

[18] S. K. Kim, W. S. Han, T. J. Kim, T. Y. Kim, S. W. Nam, M. Mitoraj, Ł. Piekoś, A. Michalak, S.-J. Hwang, S. O. Kang, *J. Am. Chem. Soc.* **2010**, *132*, 9954–9955.

[19] U. Sanyal, U. B. Demirci, B. R. Jagirdar, P. Miele, *ChemSusChem* **2011**, *4*, 1731–1739.

[20] M. Chandra, Q. Xu, *J. Power Sources* **2006**, *156*, 190–194.

[21] Q. Xu, M. Chandra, *J. Power Sources* **2006**, *163*, 364–370.

[22] J. M. Yan, X. B. Zhang, S. Han, H. Shioyama, Q. Xu, *Angew. Chem. Int. Ed.* **2008**, *47*, 2287–2289.

[23] T. Umegaki, J. M. Yan, X. B. Zhang, H. Shioyama, N. Kuriyama, Q. Xu, *Int. J. Hydrogen Energy* **2009**, *34*, 3816–3822.

[24] J. M. Yan, X. B. Zhang, T. Akita, M. Haruta, Q. Xu, *J. Am. Chem. Soc.* **2010**, *132*, 5326–5327.

[25] J. M. Yan, X. B. Zhang, H. Shioyama, Q. Xu, *J. Power Sources* **2010**, *195*,

1091–1094.

[26] T. Umegaki, J. M. Yan, X. B. Zhang, H. Shioyama, N. Kuriyama, Q. Xu, *J. Power Sources* **2010**, *195*, 8209–8214.

[27] H. L. Jiang, Q. Xu, *Catalysis Today* **2011**, *170*, 56–63.

[28] P. Z. Li, A. Aijaz, Q. Xu, *Angew. Chem. Int. Ed.* **2012**, *51*, 6753–6756.

[29] M. Yadav, Q. Xu, *Energy Environ. Sci.* **2012**, *5*, 9698–9725.

[30] Ö. Metin, S. Özkar, *Int. J. Hydrogen Energy* **2011**, *36*, 1424–1432.

[31] G. Chen, S. Desinan, R. Rosei, F. Rosei, D. Ma, *Chem. Commun.* **2012**, *48*, 8009–8011.

[32] T. Umegaki, Q. Xu, Y. Kojima, *J. Power Sources* **2012**, *216*, 363–367.

[33] L. Yang, W. Luo, G. Z. Cheng, *Catal. Lett.* **2013**, *143*, 873–880.

[34] O. Akdim, U. B. Demirci, P. Miele, *Int. J. Hydrogen Energy* **2013**, *38*, 5627–5637.

[35] M. R. Knecht, J. C. Garcia-Martinez, R. M. Crooks, *Chem. Mater.* **2006**, *18*, 5039–5044.

[36] K. A. Marvin, N. N. Thadani, C. A. Atkinson, E. L. Keller, K. J. Stevenson, *Chem. Commun.* **2012**, *48*, 6289–6291.

[37] R. L. Johnston, *Atomic and Molecular Clusters*, Taylor & Francis, London, **2002**.

[38] C. D. Wagner, W. N. Riggs, L. E. Davis, J. F. Moulder, *Handbook of X-Ray Photoelectron Spectroscopy: A Reference Book of Standard Spectra for Use In X-Ray Photoelectron Spectroscopy* (Ed.: G. E. Muilenberg), Physical Electronics Division Perkin–Elmer Corp., Minnesota, **1978**.

Chapter 5

Conclusion

In this dissertation, liquid-phase hydrogen storage materials, such as ammonia borane and hydrous hydrazine, have been catalyzed over novel heterogeneous catalysts succesufully. The liquid-phase chemical hydrogen storage materials, which have relatively high hydrogen content, could be one of the promising candidates to reduce the burdane of fossil fuels demands. Development of high-performance heterogeneous catalysts, which effectively catalyze the lquid-phase chemical hydrogen storage materials to release the hydrogen under moderate reaction condition, is also necessary to achive a hydrogen-based energy infrastructure.

(i) One-Step synthesis of magnetically recyclable Au/Co/Fe triple–layered core-shell nanoparticles as highly efficient catalysts for the hydrolytic dehydrogenation of ammonia borane:

We have developed the first one-step seeding-growth method for the synthesis of magnetic triple-layered core–shell Au/Co/Fe nanoparticles (NPs) at room temperature under ambient atmosphere. Our developped very simple method is to take advantage of the differences in the reduction potentials amang the core and shell metal salts (Au^{3+}, Co^{2+}, Fe^{3+}), where the key points is to employ a suitable redusing agent, ammonia borane (AB). The resulting triple-layered core–shell Au/Co/Fe NPs exhibit much higher catalytic activity for the hydrolytic dehydrogenation of ammonia borane than the

corresponding mono- and bi-metallic NPs due to the synergestic effects among Au, Co and Fe, come from unique electronical structures. Moreover, this simple one-step seeding-growth technique can be extended to other multi-metallic systems, which should be useful as optical, magnetic, and electrical materials as well as in heterogeneous catalysis.

(ii) Dendrimer-encapsulated bimetallic Pt-Ni nanoparticles as highly efficient catalysts for hydrogen generation from chemical hydrogen storage materials:

We have successfully synthesized bimetallic Pt-Ni dendrimer-encapsulated nanoparticles (DENs) with different Pt/Ni ratios via co-complexiatin of precursors Pt^{2+} and Ni^{2+} cations to fourth-generation hydroxyl-terminated poly(amidoamine) dendrimers (G4-OH) followed by simultaneous reduction by sodium borohydride in aqueous solution. The resultant Pt-Ni DENs have been characterized by TEM (EDS, HAADF-STEM, SEM), UV-Vis and XPS measuments. These characterization revealed very fine and monodistributed Pt-Ni bimetallic alloy NPs (average particle size: 1.1 ± 0.3 nm) encapsulated in G4OH dendrimer. Their heterogeneous catalytic applications for the liquid-phase chemical hydrogen stoge materials also have been studied. The best catalyst of the results, G4-OH($Pt_{12}Ni_{48}$) DENs exhibit excellent catalytic performances for the decomoposition of hydrous hydrazine and hydrolysis of ammonia borane.

(iii) Dendrimer-encapsulated Co nanoparticles as high-performance catalyst for hydrolysis of ammonia borane:

To reduce the cost of heterogeneous catalysts, non-noble metals have been attractive

candidates. We have successfully synthesized dendrimer encapsulated Co nanoparticles via complexation of Co^{2+} cations to internal tertiary amines of sixth-generation hydroxyl-terminated, poly(amidoamine) dendrimers (G6-OH) and reduction process by $NaBH_4$ and ammonia borane. The physical characterization results revealed that as-synthesized G6-OH(Co_{60}) DENs are very fine and homogeneous monodispersed NPs with average diameter of 1.6 ± 0.4 nm. G6-OH(Co_{60}) DENs exhibit a high-performance heterogeneous catalyst for hydrolysis of ammonia borane at room temperature compare to other Co catalyst. Additionaly, the temperature effcts for the hydrolysis of ammonia borane and durability of G6-OH(Co_{60}) also have been studied.

The above results present valuable informations for understanding liquid-phase chemical hydrogen storage materials and functional heterogeneous metallic nanocatalysts, and contribute to further research and development of the hydrogen as promising clean and renewable energy candidate.

List of Publications

Journal Publications

[1] "One-step synthesis of magnetically recyclable Au/Co/Fe triple-layered core–shell nanoparticles as highly efficient catalysts for the hydrolytic dehydrogenation of ammonia borane".

Kengo Aranishi, Hai-Long Jiang, Tomoki Akita, Masatake Haruta and Qiang Xu*

Nano Res. **2011**, *4*, 1233–1241.

[2] "Dendrimer-encapsulated bimetallic Pt-Ni nanoparticles as highly efficient catalysts for hydrogen generation from chemical hydrogen storage materials"

Kengo Aranishi, Ashish Kumar Singh and Qiang Xu*

ChemCatChem, **2013**, *5*, 2248–2252,

[3] "Dendrimer-encapsulated Co nanoparticles as high-performance catalyst for hydrolysis of ammonia borane."

Kengo Aranishi, Qi-Long Zhu and Qiang Xu*

ChemCatChem, submitted.

Conference Presentations

[1] "Metal nanoparticle-catalyzed hydrogen generation from liquid-phase chemical hydrogen-storage materials"

Kengo Aranishi, Hai-Long Jiang and Qiang Xu*

The 1st International Symposium on Advanced Nanostructured Materials for CleanEnergy (ANMCE), Poster, No. P-28, Osaka, Japan, **2011**.

[2] "高活性Au/Co/Fe三層コア・シェルナノ粒子触媒によるアンモニアボランの加水分解・水素発生反応"

荒西　研吾, 徐　強*

日本化学会第92春季年会, 一般講演, 講演番号 3F5-15, 神奈川, 2012.

[3] "Gold-based core-shell nanoparticle-catalyzed hydrogen generation from liquid-phase ammonia borane"

Kengo Aranishi, and Qiang Xu*

The 6th international conference on gold science technology and its applications (GOLD2012), Poster, No. 1P-045, Tokyo, Japan, **2012**.

[4] "Gold-based core-shell nanoparticle-catalyzed hydrogen generation from liquid-phase ammonia borane"

Kengo Aranishi, and Qiang Xu*

The post conference of the 6th international conference on gold science technology and its applications, Poster, Kyoto, Japan, **2012**.

[5] "Dendrimer-encapsulated bimetallic Pt-Ni nanoparticles as highly efficient catalysts

for hydrogen generation from hydrazine and ammonia borane”

Kengo Aranishi, and Qiang Xu*

The 63rd Conference of Japan Society of Coordination Chemistry, Poster, No. 1PF-006, Okinawa, Japan, **2013**.

Doctor Thesis, Kobe University

“Study of Metal Nanoparticle-Catalyzed Hydrogen Generation for Chemical Hydrogen Storage”, 87 pages

Submitted on January, 24th, 2014

The date of publication is printed in cover of repository version published in Kobe University Repository Kernel.